

1 **Interaction between a Cantilevered-free**
2 **Flexible Plate and Ideal Flow** [★]

3 R.M. Howell ^{*}, A.D. Lucey ^a, P.W. Carpenter ^b &
4 M.W. Pitman ^a

5 ^a*Fluid Dynamics Research Group, Curtin University of Technology, G.P.O. Box*
6 *U1987, Perth, W.A. 6845, Australia*

7 ^b*Fluid Dynamics Research Centre, School of Engineering, University of Warwick,*
8 *Coventry, CV4 7AL, U.K.*

9 **Abstract**

10 We develop a new computational model of the linear fluid-structure interaction of
11 a cantilevered flexible plate with an ideal flow. The system equation is solved via
12 numerical simulations that capture transients and allow the spatial variation of the
13 flow-structure interaction on the plate to be studied in detail. Alternatively, but
14 neglecting wake effects, we are able to extract directly the system eigenvalues to
15 make global predications of the system behaviour in the infinite-time limit. We use
16 these complementary approaches to conduct a detailed study of the fluid-structure
17 system. When the channel walls are effectively absent, predictions of the critical
18 velocity show good agreement with those of other published work. We elucidate the
19 single-mode flutter mechanism that dominates the response of short plates and show
20 that the principal region of irreversible energy transfer from fluid to structure oc-
21 curs over the middle portion of the plate. A different mechanism, modal-coalescence
22 flutter, is shown to cause the destabilisation of long plates with its energy transfer

23 occurring closer to the trailing edge of the plate. This mechanism is shown to al-
24 low a continuous change to higher-order modes of instability as the plate length is
25 increased. We then show how the system response is modified by the inclusion of
26 channel walls placed symmetrically above and below the flexible plate, the effect of
27 unsteady vorticity shed at the trailing edge of the plate, and the effect of a rigid sur-
28 face placed upstream of the flexible plate. Finally, we apply the modelling techniques
29 in a brief study of upper-airway dynamics wherein soft-palate flutter is considered to
30 be the source of snoring noises. In doing so, we show how a time-varying mean flow
31 influences the type of instability observed as flow speed is increased and demonstrate
32 how localised stiffening can be used to control instability of the flexible plate.

33 *Key words:* Fluid-structure interaction, Cantilevered-free flexible plate, Channel
34 flow, Flutter, Unsteady wake, Snoring

35 **1 Introduction**

36 The fluttering of a flag is perhaps the most ubiquitously observed interaction
37 between a solid and fluid and yet this deceptively simple physical system still
38 defies a complete understanding of its dynamics. A formal representation of
39 the canonical fluid-structure system, of which the flag-flutter configuration is
40 one example, is that of a mean flow interacting with a cantilevered flexible
41 surface embedded in the flow and aligned with its direction. This system dif-
42 fers from the flag-flutter example in that the structural forces are dominated
43 by a flexure term whereas for the flag problem this rôle is played by the ten-

* A preliminary version of this paper was presented in the 7th FSI, AE & FIV+N
Symposium, within the 2006 ASME PVP Conference in Vancouver, BC, Canada.

* Corresponding author. Email: r_m.howell@hotmail.co.uk

44 sion induced by large-amplitude motions. The phenomena studied herein may
45 be envisaged as vibrations of a fluid-loaded plate for which small-amplitude
46 motions and linear instability are the precursors of sustained flow-induced
47 finite-amplitude oscillations. While this system might seem distant from any
48 useful application, the elucidation of the rich dynamics at work in the model
49 problem is fundamental to our understanding of many real-world problems
50 in fluid-structure interaction. In this paper we develop a new and versatile
51 model of the system and then conduct an investigation of its stability to lin-
52 ear perturbations from an undisturbed mean state. We also apply our findings
53 to a particular biomechanical system, that comprising the motion of the soft
54 palate in the human upper airway. Our particular focus is on the characteri-
55 zation of energy exchanges between flow and solid within the system. We are
56 then able to show how these sum to the overall, or global, amplification or
57 decay of flexible-plate oscillations that is observed as a system response. We
58 remain aware that the present linear study cannot address the well-known
59 sub-critical instability present in such systems. However, the numerical ap-
60 proach that we describe herein can readily be extended to model non-linear
61 motions of the flexible plate.

62

63 The pioneering work of Kornecki *et al.* (1976) on the problem at hand has, over
64 the past decade or so, stimulated the major thrust in research effort that it
65 deserved. Broadly the modelling of such studies divides into one of two types;
66 the flexible plate either resides in an infinite domain of fluid - for examples, see
67 Huang (1995), Yamaguchi *et al.* (2000a), Watanabe *et al.* (2002b), Argentina
68 and Mahadevan (2005), Tang and Paidoussis (2006) and Eloy *et al.* (2007)
69 - or it is embedded in plane-channel flow - for examples, see Aurégan and
70 Depollier (1995), Guo and Paidoussis (2000), Balint and Lucey (2005) and

71 Tetlow *et al.* (2006). Clearly, the unbounded-fluid case can be regarded as the
72 limit of infinite channel height for a centrally located flexible plate. All of these
73 models predict that beyond a threshold, or critical, applied flow speed the flex-
74 ible plate loses its stability to small-amplitude disturbances through a flutter
75 mechanism. The critical mode for short plates typically comprises a combina-
76 tion of the fundamental and second *in-vacuo* eigenmodes of the cantilevered
77 flexible plate. Increasing the plate length reduces the critical speed and raises
78 the order of the *in-vacuo* eigenmodes that dominate the composition of the
79 critical mode. For a short plate the flutter mechanism can be attributed to the
80 strong effect of its finiteness that creates a phase shift between the motion of
81 the plate and the forcing fluid pressure. This results in energy transfer between
82 fluid and plate at all flow speeds. Instability sets in when the net transfer is
83 from fluid to plate; this will be demonstrated in the present paper. In contrast,
84 an *infinitely-long* flexible plate, subject to potential flow, experiences a pres-
85 sure signal that is exactly orthogonal to the plate's motion at all pre-instability
86 flow speeds and therefore does not admit irreversible energy transfer; for ex-
87 ample, see Carpenter and Garrad (1985), Crighton and Oswell (1991) and
88 the discussion of Lucey and Carpenter (1993a) for the closely related prob-
89 lem of single-sided flow over an infinitely-long flexible panel. The dynamic
90 instability to which long flexible plates succumb is a Kelvin-Helmholtz type of
91 flutter. At a sufficiently high level of fluid loading two modes coalesce to give
92 a complex-conjugate pair of wave solutions, one of which is highly amplified
93 and the other commensurately damped. At the onset of this type of flutter,
94 it is the modal coalescence that creates the phase shift between the pressure
95 signal and wall motion which allows the physical transfer of energy from the
96 fluid to the plate. Long cantilevered flexible plates, which are semi-infinite in
97 the limit of streamwise extent, therefore exhibit elements of both types of the

98 aforementioned flutter mechanisms.

99

100 The fundamental relationship between local and global instability of fluid-
101 structure systems has been systematically addressed by Doaré and de Langre
102 (2006) building upon Doaré and de Langre (2002) in which the instability of
103 a fluid-conveying pipe was studied. They show when and how local waves,
104 those predicted by a dispersion equation valid for an infinitely long domain,
105 can combine through a process of propagation and reflection in a finite system
106 to yield a global instability. In the present paper, we extract eigenmodes to
107 make predications of global behaviour. However, our numerical simulations
108 effectively model local behaviour and wave reflections through the enforce-
109 ment of the boundary conditions at each end of the flexible plate. We base
110 the descriptors ‘short’ and ‘long’ for the finite system on the value of non-
111 dimensional plate length, $\bar{L} = \rho_f L / (\rho h)$, where L is its dimensional length, ρ_f
112 is the fluid density and (ρh) is the mass per unit area of the plate. However,
113 within Doaré and de Langre’s framework of ‘from waves to modes’, the entire
114 range of \bar{L} studied herein would be considered ‘short’ in that the disturbance
115 wavelengths are of the same order as the length of the flexible plate. Thus, in
116 this paper, the investigation of spatial dependence within a global response
117 can be at sub-wavelength scales.

118

119 The present study models ideal flow but can incorporate the effect of channel
120 walls. The explicit omission of viscous effects may seem an extreme assump-
121 tion. However, the use of unsteady laminar flow in Balint and Lucey (2005)
122 revealed that the flutter instability of a short flexible plate was qualitatively
123 very similar to that predicted using ideal flow. The flow solution used by Balint
124 and Lucey (2005) is restricted to flows at low Reynolds number whereas an

125 ideal-flow model can be considered as a model for flows at very high, indeed
126 infinite, Reynolds number. Like the majority of previous studies we assume
127 a two-dimensional flow-structure system that has infinite span. The elegant
128 analysis of Eloy *et al.* (2007) quantified the effect of finite span on plane waves
129 with fronts perpendicular to the flow direction; what results is a correction fac-
130 tor on the pressure field yielded by a two-dimensional analysis. Thus, we can
131 infer that the dynamics predicted by two-dimensional models will have, at
132 the very least, qualitative validity. The system studied herein is closest to the
133 plane-channel configuration investigated in Guo and Paidoussis (2000). We
134 extend their work by modelling the effects of: (a) a central rigid surface at the
135 leading edge of the flexible plate; (b) the singularity present at the leading
136 edge of the flexible plate; (c) spatially varying stiffness in the flexible plate;
137 (d) the wake shed by the motion of the flexible plate; and (e) an unsteady
138 mean flow. We also compare our findings with those from the corresponding
139 unbounded-flow study of Tang and Paidoussis (2006, 2007) who have investi-
140 gated the foregoing points (b) and (d).

141

142 The most significant difference between the present study and those that have
143 preceded it lies in our development and use of a computational model that
144 permits us to conduct numerical simulations of the flow-structure system. This
145 means that we make no presupposition about disturbance form; by contrast,
146 modal studies require that the fluid-loaded deformation of the flexible plate
147 can be constructed accurately from a finite number of pre-selected *in-vacuo*
148 plate modes. Our approach also permits us to model transient behaviour that
149 exists prior to a system eigen-state being reached or that results from the
150 use of a time-varying mean flow. We are also able to identify spatially lo-
151 calised dynamics within the system. These are lost in the aggregating process

152 of Galerkin, or modal, methods that only generate global predictions of be-
153 haviour and stability.

154

155 The geometry modelled is shown in Fig. 1. Ideal flow is assumed and the per-
156 turbed flow field modelled using a linearised boundary-element method, that
157 then yields the perturbation pressure acting on the plate through the linearised
158 unsteady Bernoulli equation. The motion of the flexible-plate is modelled us-
159 ing linearised one-dimensional beam theory. The unsteady shed vorticity is
160 modelled using a linearised discrete-vortex method. In the boundary-element
161 method, vortex singularities are used to model the central surface as they cap-
162 ture the discontinuity in tangential velocity across this surface. Although Tang
163 and Païdoussis (2007) recently used a lumped-vortex method ours is the first
164 time that a continuous vortex distribution has been used for a fully-coupled
165 flow-structure interaction for arbitrarily-deforming lifting-surfaces. The as-
166 sembled system is then used to conduct a variety of numerical simulations,
167 the results of which map out the response space of the system. However,
168 we also use the computational model to extract directly the eigenmodes of
169 the fluid-structure system using the state-space methods developed by Lucey
170 and Pitman (2006). An equivalent approach was adopted by Argentina and
171 Mahadevan (2005) although they made simplifying assumptions in their flow
172 model in order to develop a tractable system equation. Our computational
173 model allows the full description of fluid loading to be included. Moreover,
174 the accuracy of our system-stability results is ensured because we include all
175 M fluid-structure eigenmodes, where M is the number of collocation points
176 on the plate. Increasing M decreases the error at a monotonically reducing
177 rate as the solution converges to being exact at the limit $M = \infty$.

178

179 The paper is laid out as follows. Initially the construction of the numeri-
180 cal model is described and diagnostic variables are introduced. Results from
181 our numerical simulations are then presented that analyse the flutter instabil-
182 ities observed at low and high mass ratios. Predicted critical-velocity values
183 obtained via our numerical simulations and from other published work are
184 then compared. Further results are then presented that demonstrate the ef-
185 fects on the flutter instability of shed vorticity, a central rigid-surface at the
186 leading edge of the flexible plate, channel walls, an unsteady mean-flow and
187 distributed stiffness in the flexible plate. The mechanism of all flutter instabil-
188 ities observed is explained in terms of the transfer of fluid energy to the plate
189 via the interaction of the fluid pressure and the plate velocity.

190 2 Theoretical and Computational Modelling

191 The mechanics of the disturbed, linear flow-structure system may be repre-
192 sented by an equation of motion of the form

$$[L]\eta = -\delta p(\ddot{\eta}, \dot{\eta}, \eta), \quad (1)$$

193
194 subject to initial values and plate-edge conditions. $[L]$ is a differential operator
195 on the vertical plate displacement, η . δp is the pressure perturbation due to
196 disturbances to the free-stream flow, U_∞ , and is composed of hydrodynamic
197 stiffness, damping and inertia. Co-ordinate axes are as shown in Fig. 1 and
198 Fig. 2 shows how the surfaces of the structure are discretised into a set of
199 boundary-elements or panels where M_w , M_{cs} and M are the number of panels
200 on the channel walls, rigid central-surface and the flexible plate respectively.
201 At the centre of each panel is a control point where properties relating to the

202 fluid pressure calculated for each panel are assumed to be located. In contrast,
 203 the flexible plate is discretised into a set of $N(= M - 1)$ mass points where the
 204 mechanical properties of the plate will be assumed centred; these are defined
 205 by the panel end-points as shown in Fig. 2. Below, we describe the separate
 206 plate and flow models and how they are coupled into the final computational
 207 model.

208 *2.1 Plate Mechanics*

209 The specific spatially-discretised form of Eq. (1) for a thin flexible plate is

$$\rho h \ddot{\eta}_n + d \dot{\eta}_n + B \nabla^4 \eta_n = -\delta p_n, \quad (2)$$

210

211 where n is the mass-point number along the flexible plate. ρ , h , d and B are
 212 respectively the density, thickness, damping coefficient and flexural rigidity of
 213 the plate. The flexural rigidity is related to the elastic modulus, E , and the
 214 Poisson ratio, ν , through

$$B = \frac{Eh^3}{12(1-\nu^2)}. \quad (3)$$

215

216 The flexure term $\nabla^4 \eta_n$ is the fourth-order spatial derivative of η_n and can be
 217 written in (central) finite-difference form as

$$\nabla^4 \eta_n = \frac{6}{\delta x^4} \eta_n - \frac{4}{\delta x^4} (\eta_{n-1} + \eta_{n+1}) + \frac{1}{\delta x^4} (\eta_{n-2} + \eta_{n+2}). \quad (4)$$

218

219 where δx is the panel length; for the uniform discretisation used in this paper,
 220 $\delta x = L/M$ where L is the length of the flexible plate. Equation (2) can be
 221 rewritten in matrix form as

$$\rho h [\mathbf{I}] \{\ddot{\eta}\} + d [\mathbf{I}] \{\dot{\eta}\} + B [\mathbf{D}_4] \{\eta\} = -\{\delta p\}, \quad (5)$$

222

223 where $[\mathbf{I}]$ is the identity matrix and $[\mathbf{D}_4]$ is a pentadiagonal matrix containing
 224 the terms generated by Eq. (4). Cantilevered-free edge conditions are enforced
 225 on the plate by imposing zero displacement and gradient at the cantilevered
 226 end (the leading edge) and zero bending moment and shear force at the free
 227 end (the trailing edge); these conditions are implicit in the construction of
 228 $[\mathbf{D}_4]$ via their application at the *dummy nodes* labelled $N = -2, -1, N + 1$
 229 and $N + 2$ illustrated in Fig. 2. Our numerical model of a cantilevered-free
 230 plate has been validated by comparing angular frequencies of oscillation of the
 231 first six *in-vacuo* eigenmodes, as predicted by theory and our computational
 232 model; the results of this validation are similar to those presented in Balint
 233 and Lucey (2005).

234 2.2 Fluid Mechanics

235 To calculate the magnitude of the pressure acting on the structural surfaces
 236 that is generated by the deflection of the plate, a linearised boundary-element
 237 method (BEM) of flow solution is employed. To apply the BEM, a surface
 238 is discretised into a finite number of panels; at the centre of these panels is
 239 the panel *control point*. Singularities are distributed along these panels; by
 240 determining the strengths of these singularities the pressure at the individual
 241 control points can then be calculated. The discretisation and singularity dis-
 242 tributions utilised in our methodology are illustrated in Fig. 2. We use vortex
 243 singularities to model the central surface as they capture the discontinuity in
 244 tangential velocity across this lifting surface. In contrast, source/sink singu-

245 larities are used to model the channel walls as these are non-lifting surfaces.
 246 The linearisation of the BEM is also illustrated in this figure: the BEM panels
 247 remain fixed on the horizontal, whereas the mass points of the plate are free
 248 to travel in the vertical axis. Respectively, the velocity perturbations and per-
 249 turbation potentials at any control point i on the flexible plate *only* are given
 250 by

$$u_i^{T'} = \sum_{m=1}^{M_w} I_{im}^{T\sigma} \sigma_m + \sum_{m=1}^{M_{cs}+M} I_{im}^{T\gamma} \gamma_m + \sum_{m=1}^{M_{cs}+M} I_{im}^{T\lambda} \lambda_m, \quad (6)$$

$$\Phi_i = \sum_{m=1}^{M_w} I_{im}^{\phi\sigma} \sigma_m + \sum_{m=1}^{M_{cs}+M} I_{im}^{\phi\gamma} \gamma_m + \sum_{m=1}^{M_{cs}+M} I_{im}^{\phi\lambda} \lambda_m, \quad (7)$$

251

252 where I_{im}^T and I_{im}^ϕ are sets of time-independent influence coefficients that quan-
 253 tify the influence of panel m on panel i . γ_m and λ_m are respectively the zero-
 254 order and first-order vortex strengths distributed along the central surface
 255 and σ_m are the zero-order source/sink strengths distributed along the chan-
 256 nel walls. To solve for the singularity strengths, a von Neumann boundary-
 257 condition is applied so that

$$\begin{Bmatrix} \Gamma_m \\ \dots \\ \sigma_m \end{Bmatrix} = [I_{im}^N]^{-1} \{U_\infty \theta_m + \dot{\eta}_m + u_m^{Nb}\}, \quad (8)$$

258

259 where $\Gamma_m = \gamma_m + \lambda_m$. $[I_{im}^N]^{-1}$ contains, in addition to the normal influence-
 260 coefficients of the singularities, the boundary conditions of: a) vortex strength
 261 continuity at panel end points; and b) zero vorticity at the plate's trailing
 262 edge (thus enforcing the standard Kutta condition for linear displacements of
 263 zero pressure difference at the trailing edge). The term θ_m is the panel's angle

264 to the horizontal; as the model is linearised, this can be found through

$$\theta_m = \frac{(\eta_{m+1} - \eta_m)}{\delta x}, \quad (9)$$

265

266 where $n = m - 1$. The term $\dot{\eta}_m$ is the panel's vertical speed and u_m^{Nb} is the
 267 normal velocity induced by the vortex blobs that model the wake; the latter
 268 term is derived below. With the application of the Kutta condition, the effect
 269 of the steady vortical wake behind the plate is taken into account. At $t = 0$,
 270 the total vorticity in the system, ζ , is equal to that bound in the plate and
 271 hence

$$\zeta^{t=0} = \sum_{i=1}^{M_{cs}+M} \gamma_i^{t=0} \delta x_i. \quad (10)$$

272

273 In Eq. (10), it is noted that the zero-order, vortex singularity-strengths from
 274 the panel method, γ_i , (first referred to in Eq. (6)) are in units of vorticity
 275 per-unit-length; hence the terms γ_i are multiplied by their respective panel
 276 lengths δx_i to obtain the addition of each panel to the bound vorticity. Owing
 277 to the movement of the flexible plate the bound vorticity changes with time;
 278 the physical effect of this change is to generate an unsteady wake of shed
 279 vorticity, its source is the trailing edge of the flexible surface. To model this
 280 wake we release a point vortex of strength γ^b (a *vortex blob*) at each time step.
 281 Therefore, at any future time t the total vorticity in the system will be equal
 282 to the total bound vorticity at that time and any shed vorticity in the wake
 283 generated up to that point; hence

$$\zeta^t = \underbrace{\sum_{i=1}^{M_{cs}+M} \gamma_i^t \delta x_i}_{\text{bound vorticity at } t} + \underbrace{\sum_{i=1}^{N^b-1} \gamma_i^b}_{\text{shed vorticity at } t-1}, \quad (11)$$

284

285 where N^b is the total number of blobs present in the wake. In Eq. (11), the blob

286 strengths, γ_i^b , are already in units of vorticity because they are the strengths of
 287 point vortices. The strength of the blob to be released at time t , $\gamma_{N^b}^b$, is chosen
 288 so that the Kelvin condition (that there should be no change in the total
 289 vorticity in the system with time), is enforced at each time step. Therefore
 290 $\gamma_{N^b}^b$ is equal to the difference between Eqs. (10) and (11); hence

$$\gamma_{N^b}^b = \sum_{i=1}^{M_{cs}+M} \gamma_i^{t=0} \delta x_i - \left(\sum_{i=1}^{M_{cs}+M} \gamma_i^t \delta x_i + \sum_{i=1}^{N^b-1} \gamma_i^b \right). \quad (12)$$

291

292 It is assumed in this model that the strength of the blobs do not diminish with
 293 time. The effect of the shed blobs on the panels (and each other) is calculated
 294 using a discrete-vortex method similar to that detailed in Chorin (1973). In
 295 this method the blobs are governed by the two-dimensional Poisson equation
 296 such that

$$\nabla^2 \psi = -\omega(\underline{x}, t) = -\sum_{n=1}^{N_b} f_{\alpha_n}(\underline{r}_n) \gamma_n^b, \quad (13)$$

297

298 where ψ is the stream function, $\omega(\underline{x}, t)$ is the two-dimensional vorticity field,
 299 $f_{\alpha_n}(\underline{r}_n)$ is the blob core function and \underline{r}_n is the vector between a blob and the
 300 point p that is anywhere in the infinite space away from the blob. A Gaussian
 301 approach is used for the core function; this utilises a core size, α_n , for each
 302 blob so that the blobs can be coincident without creating a singular result.
 303 The Gaussian core function utilised is

$$f_{\alpha_n}(\underline{r}_n) = \frac{1}{\alpha_n^2 \pi} e^{-\frac{|\underline{r}_i - \underline{r}_n|^2}{\alpha_n^2}}, \quad (14)$$

304

305 where \underline{r}_i is the distance between a point i on the flexible plate and the point p
 306 in space. Utilising Eq. (13) and Eq. (14), the discretised form for the velocity
 307 induced at a point i , \underline{u}_i^b , owing to the n^{th} blob is

$$\underline{u}_i^b = -\frac{\partial\psi}{\partial r} = u_i^{Tb}\underline{i} + u_i^{Nb}\underline{j}, \quad (15)$$

308 where

$$u_i^{Tb} = -\gamma_n^b \frac{y_n}{2\pi|\underline{r}_i - \underline{r}_n|^2} \left(1 - e^{-\frac{|\underline{r}_i - \underline{r}_n|^2}{\alpha_n^2}} \right), \quad (16)$$

$$u_i^{Nb} = \gamma_n^b \frac{x_n}{2\pi|\underline{r}_i - \underline{r}_n|^2} \left(1 - e^{-\frac{|\underline{r}_i - \underline{r}_n|^2}{\alpha_n^2}} \right), \quad (17)$$

309

310 where x_n and y_n are the horizontal and vertical components of \underline{r}_n respectively;
 311 \underline{i} and \underline{j} denote the cartesian components of \underline{u}_i^b . A linearised version of the shed
 312 vorticity model is deployed in this paper with the blobs assumed only to travel
 313 horizontally. Therefore the tangential component of the blob velocity, u_i^{Tb} , is
 314 zero because y_n is zero; this leads to large computational savings allowing de-
 315 tailed numerical simulations to be executed on a standard desktop computer.
 316 In the present application, the magnitude of core size is assumed the same for
 317 each blob and is chosen to be $\alpha = 0.4$. Each blob, when created, has its centre
 318 placed at a distance of $U_\infty \delta t$ from the trailing edge of the plate where δt is
 319 the size of the time step; this is also the assumed distance each blob travels
 320 between time steps.

321 2.3 Fluid-structure Coupling

322 In Lucey *et al.* (1998) it is shown that when a rotational wake is added to a
 323 general flow-structure interaction where the flow is irrotational, the fluid in the
 324 region close to the plate remains predominantly irrotational as the rotational
 325 fluid is mainly downstream of the trailing edge of the plate. It should be noted
 326 however, that the rotational wake does contribute to the determination of the
 327 velocity field adjacent to the moving plate in much the same way that vortex

328 singularities can be used in models of ideal flow with circulation. Therefore
 329 the pressure along the flexible plate can be calculated via the discretised form
 330 of the linearised unsteady Bernoulli equation; the pressure difference *across*
 331 the plate can be obtained, assuming that the pressure is equal and opposite
 332 in value on the upper and lower surfaces of the plate, by multiplying this
 333 equation by a factor of two so that we have

$$\delta p_i = -2\rho_f U_\infty u_i^{T'} - \rho_f \frac{\partial \Phi_i}{\partial t}, \quad (18)$$

334

335 where ρ_f is the free-stream fluid density. There is no evidence in Eq. (18) that
 336 the second part of the pressure has been multiplied by a factor of two; this
 337 owes itself to the method employed of calculating Φ_i , given by Eq. (7), that
 338 automatically accounts for the pressure difference across the plate with no
 339 further alteration. Inserting Eqs. (6), (7), (8) and (15) into Eq. (18), gives

$$\begin{aligned} \{\delta p_i\} = -\rho_f \left(\underbrace{2U_\infty'^2 [I_{im}^T] [I_{im}^N]^{-1} \{\theta_m\} + \dot{U}_\infty' [I_{im}^\phi] [I_{im}^N]^{-1} \{\theta_m\}}_{\text{Hydrodynamic Stiffness}} \right. \\ + \underbrace{2U_\infty' [I_{im}^T] [I_{im}^N]^{-1} \{\dot{\eta}_m^{av} - u_m^{Nb}\}}_{\text{Hydrodynamic Damping I}} + \underbrace{[I_{im}^\phi] [I_{im}^N]^{-1} \{U_\infty' \dot{\theta}_m\}}_{\text{Hydrodynamic Damping II}} \\ \left. + \underbrace{[I_{im}^\phi] [I_{im}^N]^{-1} \{\ddot{\eta}_m - \dot{u}_m^{Nb}\}}_{\text{Hydrodynamic Inertia}} \right), \quad (19) \end{aligned}$$

340

341 where $U_\infty' = U_\infty + A \sin \omega t$ (allowing the incorporation of an unsteady mean
 342 flow) and

$$\dot{\eta}_m^{av} = 0.5(\dot{\eta}_n + \dot{\eta}_{n+1}). \quad (20)$$

343

344 The coupled wall-flow system is assembled by introducing the pressure of
 345 Eq. (19) into the right-hand side of Eq. (5). Therefore, we have

$$\begin{aligned}
& \rho h [\mathbf{I}] \{\ddot{\eta}_m\} + d [\mathbf{I}] \{\dot{\eta}_m\} + B [\mathbf{D}_4] \{\eta_m\} = \\
& 2\rho_f U'_\infty \frac{1}{\delta x} [\mathbf{B}_1^+] \{\eta_m\} + \rho_f \dot{U}'_\infty \frac{1}{\delta x} [\mathbf{B}_2^+] \{\eta_m\} + \rho_f U'_\infty \frac{1}{\delta x} [\mathbf{B}_2^+] \{\dot{\eta}_m\} \\
& + \rho_f U'_\infty [\mathbf{B}_1^-] \{\dot{\eta}_m\} + \rho_f [\mathbf{B}_2] \{\ddot{\eta}_m\} - 2\rho_f U'_\infty [\mathbf{B}_1] \{u_m^{Nb}\} - \rho_f [\mathbf{B}_2] \{\dot{u}_m^{Nb}\}, \quad (21)
\end{aligned}$$

346

347 where the $[\mathbf{B}]$ matrices are suitably rearranged forms of the influence matrices
348 presented in Eq. (19) to allow, via the use of the relations in Eqs. (9)
349 and (20), the expression of the fluid-structure system solely in terms of plate
350 acceleration, velocity and displacement and blob acceleration and velocity.
351 The hydrodynamic pressures computed using Eq. (19) are evaluations at the
352 control points of the plate panels, whereas the pressures in Eq. (5) are calculated
353 at the mass points; this introduces a small numerical error that reduces
354 as the discretisation of the plate is increased. Equation (21) can be re-arranged
355 to give the system equation

$$\{\ddot{\eta}_m\} = [\mathbf{E}] \{\dot{\eta}_m\} + [\mathbf{F}] \{\eta_m\} - [\mathbf{G}] \{u_m^{Nb}\} - [\mathbf{H}] \{\dot{u}_m^{Nb}\}, \quad (22)$$

356 where

$$[\mathbf{E}] = \left[\rho h [\mathbf{I}] - \rho_f [\mathbf{B}_2] \right]^{-1} \left[2\rho_f U'_\infty [\mathbf{B}_1^-] + \rho_f U'_\infty \frac{1}{\delta x} [\mathbf{B}_2^+] - d [\mathbf{I}] \right], \quad (23)$$

$$[\mathbf{F}] = \left[\rho h [\mathbf{I}] - \rho_f [\mathbf{B}_2] \right]^{-1} \left[2\rho_f U'^2_\infty \frac{1}{\delta x} [\mathbf{B}_1^+] + \rho_f \dot{U}'_\infty \frac{1}{\delta x} [\mathbf{B}_2^+] - B [\mathbf{D}_4] \right], \quad (24)$$

$$[\mathbf{G}] = \left[\rho h [\mathbf{I}] - \rho_f [\mathbf{B}_2] \right]^{-1} \left[2\rho_f U'_\infty [\mathbf{B}_1] \right], \quad (25)$$

$$[\mathbf{H}] = \left[\rho h [\mathbf{I}] - \rho_f [\mathbf{B}_2] \right]^{-1} \left[\rho_f [\mathbf{B}_2] \right]. \quad (26)$$

357 2.4 Solution Methods

358 Two distinct, but complementary, approaches are used to solve the system
359 equation. In the first, a time-stepping numerical integration is performed to

360 yield numerical simulations of the system response to an initial form of im-
 361 posed excitation. Such simulations are able to capture transient effects and
 362 permit localised dynamics to be investigated through the analysis of a series
 363 of numerical experiments. However, this approach is not so well suited to the
 364 prediction of long-time system response and its global mapping. Thus, for the
 365 second approach we assume a single-frequency system response that might be
 366 expected in the infinite-time limit after all transient oscillations of the plate
 367 have decayed. We are then able to use a state-space method that permits the
 368 direct extraction of the fluid-structure eigenmodes from the system equation.

369

370 The numerical simulations presented in this paper are produced using a semi-
 371 implicit method of solution of Eq. (22); this applies Gauss-Siedel sweeps over
 372 the internal mass points, utilising the following simplified predictor-corrector
 373 relations

$$\{\dot{\eta}_i^{t+\delta t}\} \approx \{\dot{\eta}_i^t\} + \delta t \frac{\{\ddot{\eta}_i^t + \ddot{\eta}_i^{t+\delta t}\}}{2} \quad (27)$$

$$\{\eta_i^{t+\delta t}\} \approx \{\eta_i^t\} + \delta t \frac{\{\dot{\eta}_i^t + \dot{\eta}_i^{t+\delta t}\}}{2}, \quad (28)$$

374

375 to yield converged values of acceleration, velocity and displacement for every
 376 mass point at each time step in the evolution of the disturbed system.

377

378 Global predictions of the infinite-time system behaviour are generated using
 379 a standard state-space method, implemented in a similar way to that detailed
 380 by Lucey and Pitman (2006). As applied in this paper, we do not incorpo-
 381 rate the effects of the downstream wake nor of an unsteady free-stream. The
 382 matrices in Eq. (22) are re-arranged as a *companion-form* matrix from which
 383 the eigenvalues and vectors of the coupled system can be extracted directly

384 and the values of critical velocity can be identified. Thus re-writing Eq. (22),
 385 having neglected the wake terms, we have

$$\left\{ \frac{d^2 \eta_m}{dt^2} \right\} - [\mathbf{E}] \left\{ \frac{d\eta_m}{dt} \right\} - [\mathbf{F}] \{\eta_m\} = 0. \quad (29)$$

386

387 The following substitutions are made

$$w_1(t) = \eta(t) \quad \text{and} \quad w_2(t) = \frac{d\eta}{dt} = \dot{w}_1(t). \quad (30a, b)$$

388

389 Inserting relations Eq. (30a) and Eq. (30b) into Eq. (29) yields

$$\{\dot{w}_2\} - [\mathbf{E}] \{w_2\} - [\mathbf{F}] \{w_1\} = 0. \quad (31)$$

390

391 Rearranging Eq. (31) for \dot{w}_2 we have

$$\{\dot{w}_2\} = [\mathbf{F}] \{w_1\} + [\mathbf{E}] \{w_2\}. \quad (32)$$

392

393 Equations (30) and (32) lead to a system state equation

$$\begin{pmatrix} \dot{w}_1 \\ \dot{w}_2 \end{pmatrix} = \begin{bmatrix} 0 & I \\ F & E \end{bmatrix} \begin{pmatrix} w_1 \\ w_2 \end{pmatrix}, \quad (33)$$

394

395 that is more simply expressed as

$$\dot{w} = [H]w, \quad (34)$$

396

397 where $[H]$ is the companion matrix. Single-frequency response is then assumed

398 and thus

$$\{w\} = \{W\} \exp(\omega t), \quad (35)$$

399

400 where ω is a complex eigenvalue of $[H]$ and $\{W\}$ is the eigenvector corre-
 401 sponding to ω that is used to generate the displacement of the plate. Thus

$$\omega = \omega_R + i\omega_I \quad \text{and} \quad W = W_R(x) + iW_I(x). \quad (36a, b)$$

402 To calculate the plate displacement $\{\eta\}$, only the real part of the first N terms
 403 of $\{w\}$ are required; this is found by substituting Eq. (36a) and Eq. (36b) into
 404 Eq. (35) giving

$$\eta = \Re(w) = \exp(\omega_R t) (W_R(x) \cos(\omega_I t) - W_I(x) \sin(\omega_I t)). \quad (37)$$

405 2.5 Diagnostics

406 To assist in the interpretation of the results presented in this paper, defini-
 407 tions of diagnostic variables are now made. The physical significance of these
 408 variables is detailed in the results section when they are used to investigate
 409 the fluid-structure phenomena encountered. It is shown in Balint and Lucey
 410 (2005) that multiplying Eq. (5) by $\dot{\eta}$ and then integrating over the length of
 411 the flexible plate yields the following energy-evolution equation for the fluid-
 412 loaded plate

$$\frac{d}{dt} \left(\underbrace{\frac{1}{2} \rho h \int_0^L \dot{\eta}^2 dx}_{E_k} + \underbrace{\frac{1}{2} B \int_0^L \eta_{,xx}^2 dx}_{E_s} \right) = \underbrace{\int_0^L (-\delta p) \dot{\eta} dx}_{\dot{W}} - \underbrace{d \int_0^L \dot{\eta}^2 dx}_{\dot{D}}, \quad (38)$$

413

414 where E_s and E_k are the strain and kinetic energies of the flexible plate re-
 415 spectively and the total energy, E_t , is equal to $E_s + E_k$. \dot{W} and \dot{D} are respec-
 416 tively the rate of work done by the fluid in the flexible plate and the energy-
 417 dissipation rate by structural damping within the plate. The total work done

418 over a particular time period t_p is $W(t_p) = \int_0^{t_p} \dot{W}(t) dt$. Both $E_t(t_p)$ and $W(t_p)$
 419 are plotted in non-dimensional form

$$\bar{E}_t(t_p) = \frac{E_t(t_p)}{E_s(0)} \quad \text{and} \quad \bar{W}(t_p) = \frac{W(t_p)}{E_s(0)}. \quad (39a, b)$$

420

421 Time, free stream velocity and plate damping are non-dimensionalised using
 422 the method described in Crighton and Oswell (1991) for an isolated, infinitely-
 423 long flexible-surface so that

$$\bar{t} = t \frac{\rho_f^2 B^{\frac{1}{2}}}{(\rho h)^{\frac{5}{2}}}, \quad \bar{U} = U_\infty \frac{(\rho h)^{\frac{3}{2}}}{\rho_f B^{\frac{1}{2}}} \quad \text{and} \quad \bar{d} = d \frac{(\rho h)^{\frac{3}{2}}}{\rho_f^2 B^{\frac{1}{2}}}. \quad (40a, b, c)$$

424

425 In the present study the flexible surface is not infinitely long, nor is it isolated
 426 and thus two further non-dimensional parameters are required; these are the
 427 non-dimensional length (or mass ratio), \bar{L} , and the non-dimensional channel
 428 height, \bar{H} , defined by

$$\bar{L} = \frac{\rho_f L}{\rho h} \quad \text{and} \quad \bar{H} = \frac{H}{L}, \quad (41a, b)$$

429 where H is the distance from the central surface to either channel wall (the
 430 half channel height, $H/2$, defined in Fig. 1). Thus in the absence of structural
 431 damping the three control parameters for the fluid-structure system are \bar{U} , \bar{L}
 432 and \bar{H} . When plotting data we use the following non-dimensional forms

$$\bar{\eta} = \frac{\eta}{\eta_0}, \quad \bar{x} = \frac{x}{L}, \quad \bar{\delta p} = \frac{\delta p}{\rho_f U_\infty^2}, \quad \bar{\dot{\eta}} = \frac{\dot{\eta}}{U_\infty}, \quad \bar{\omega} = \omega \frac{(\rho h)^{\frac{5}{2}}}{\rho_f^2 B^{\frac{1}{2}}}, \quad (42a, b, c, d, e)$$

433

434 where η_0 is the maximum value of η when the plate is initially deflected to
 435 provide excitation to the fluid-structure system. ω is the angular frequency
 436 of oscillation of the flexible surface and it is non-dimensionalised using the
 437 scheme adopted for time in Eq. (40a); however a second scheme of non-

438 dimensionalisation of ω , $\bar{\omega}$, is used in the following discussion where ω is
439 divided by the angular frequency of oscillation of the second *in-vacuo* eigen-
440 mode, ω_2

$$\bar{\omega} = \frac{\omega}{\omega_2}. \quad (43)$$

441

442 This permits an easier physical grasp of the effect of the fluid loading on the
443 oscillations of the flexible-plate.

444 3 Results

445 We first present results for the much-studied case of an isolated flexible plate.
446 This requires moving the upper and lower walls apart until they no longer
447 influence the system dynamics; a value of $\bar{H} = 1$ is shown to achieve this, see
448 Howell *et al.* (2004). This leaves just two control parameters, \bar{U} and \bar{L} , that
449 determine the system response. Our goal is to find the critical flow speed, \bar{U}_c ,
450 beyond which flutter first sets in and identify the mechanism that causes the
451 unstable behaviour. We then explore variations to critical speed and instabil-
452 ity mechanism from this ‘standard case’ that occur through the introduction
453 of: a) an unsteady wake, b) a rigid inlet-surface, c) channels walls, d) tem-
454 poral variation of the mean flow, and e) variable plate stiffness. The last two
455 variations are presented with reference to human snoring.

456

457 Although all results are presented within the non-dimensional framework of
458 §2.5 above, illustrative physical properties used in §3.1 and §3.2 are $L =$
459 1.355 m , $\rho = 2710 \text{ kg/m}^3$, $h = 0.5 \text{ mm}$, $E = 7 \times 10^7 \text{ N/m}^2$, $d = 9.08 \times$
460 10^{-2} Ns/m^3 ; therefore, to give $\bar{L} = 1$ a value of $\rho_f = 1 \text{ kg/m}^3$ is required.

461 Variations to \bar{L} were effected by varying ρ_f ; this permits a fixed discretisa-
 462 tion, $M = 50$, of the flexible-plate to be used that maintains constant numer-
 463 ical accuracy. The numerical simulations require an initial excitation to the
 464 fluid-structure system. This is provided by releasing the flexible plate from an
 465 imposed deflection at $t = 0$. The deflection form used is that of the second
 466 *in-vacuo* eigenmode of the cantilevered-free plate. Of course, any other initial
 467 form could have been used to the same effect after the passage of sufficient
 468 time. We have chosen this mode because, it will be shown, it bears a close
 469 resemblance to the critical mode for low \bar{L} and thereby reduces the time taken
 470 for the system to arrive at its quasi-steady state.

471 3.1 Isolated flexible plate: $0.2 \leq \bar{L} \leq 1000$, $\bar{H} = 1$

472 We first consider the case of $\bar{L} = 1$. Figure 3(a) shows the system eigenvalues
 473 obtained using our state-space method. We have plotted just the two eigen-
 474 values with the lowest frequencies although all $M = 50$ eigenmodes of the
 475 system are present in the calculation. Thus, there is no *a priori* selection of
 476 modes that contribute most strongly to the system solution. The morphology
 477 of the state-space is similar to that obtained by Guo and Paidoussis (2000) and
 478 Eloy *et al.* (2007). We note the second mode (marked 2) of the fluid-structure
 479 system is the first to become unstable, $\bar{\omega}_R > 0$ for $\bar{U} > \bar{U}_c = 5.452$, with a
 480 non-zero oscillation frequency, $\bar{\omega}_I$, that indicates flutter. Thus, the magnitude
 481 of the restorative structural force of the plate exceeds that of pressure loading
 482 throughout the flow-speed range. In contrast, for the first mode (marked 1)
 483 there is a range of flow speeds for which the flexible plate adopts a mode shape
 484 (not presented in this paper) in which its restorative forces almost exactly

485 balance the pressure loading and non-oscillatory damped behaviour occurs.
 486 For flexible plates held at both ends, this type of force balance leads to the
 487 onset of divergence instability. In the present cantilevered-free configuration
 488 its negative $\bar{\omega}_R$ throughout the flow-speed range means that Mode 1 would
 489 not feature in the long-term response of the physical system. Figure 3(b)
 490 shows the corresponding system eigenvalues when some damping, $\bar{d} = 5$, is
 491 present. Contrasting this with the elastic-plate result of Fig. 3(a), it is seen
 492 that while second-mode flutter continues to be the critical instability, its onset
 493 flow speed has been significantly increased. The fact that energy dissipation
 494 through damping can be used to control the instability strongly suggests that
 495 the flutter mechanism owes itself to the rate of irreversible energy transfer
 496 from flow to structure. This will be confirmed in the investigation that follows
 497 immediately below.

498
 499 We now focus on the form and cause of the flutter instability seen in Fig. 3 for
 500 $\bar{L} = 1$. Figures 4(a)-(c) show results obtained at the critical speed for which
 501 $\bar{U} = 5.452$. The oscillation of the plate is depicted in Fig. 4(a) as a sequence
 502 of snapshots of the flexible plate. An oscillatory, neutrally stable, steady-state
 503 evolves from the markedly different shape of the initial excitation. It can be
 504 shown, using a Fourier analysis, that this critical mode can be made up of
 505 33% and 63% of the first two *in-vacuo* eigenmodes based upon strain-energy
 506 content, the remainder coming from higher-order modes. The dominant contri-
 507 bution of the first two *in-vacuo* modes in combination accounts for the necking
 508 seen in the envelope of oscillation. The value of $\bar{\omega}$ for this critical mode is 0.69;
 509 the effect of the fluid is therefore to reduce the plate's angular frequency of
 510 oscillation from that of the second *in-vacuo* mode by 31%. Figure 4(b) shows
 511 that after an initial drop in the plate's total energy, \bar{E}_t , associated with its

512 evolution from the applied initial condition to system eigenstate, a steady
513 state is achieved. This confirms the neutral stability of the plate's oscillation
514 at this critical speed.

515

516 We now consider the energy transfers that underpin this time-series of the
517 plate's energy. Figures 4(c) and (d) respectively show the time-variation of
518 the work done by the fluid-flow on the plate for two cases: exactly at the crit-
519 ical speed ($\bar{U}_c = 5.452$) and at just above the critical speed ($\bar{U} = 6.0$). In each
520 case, the total work done on the entire length of the flexible plate is plotted
521 and the work done in each of the four quarters $\bar{x} : 0 \rightarrow 0.25$, $\bar{x} : 0.25 \rightarrow 0.5$,
522 $\bar{x} : 0.5 \rightarrow 0.75$ and $\bar{x} : 0.75 \rightarrow 1$, of the plate that when summed yield the
523 total. This breakdown, into just four quarters, gives a broad indication of how
524 energy transfer varies along the plate. At the critical speed it is seen that the
525 work done is negative at early times; the energy transfer is from plate to fluid
526 as the deformation evolves from that of the initial condition. Thereafter the
527 change to the mean value of total work done is zero; this again confirms the
528 neutral stability of the system at $\bar{U} = \bar{U}_c = 5.452$. However, we also note that,
529 in the steady state, energy transfer *to* the middle part of the plate (second
530 and third quarters) continuously occurs while for the downstream (fourth)
531 quarter there is energy transfer *from* the plate to the fluid that exactly coun-
532 terbalances the former. It is the combination of these local effects that yields
533 the global neutral stability of the mode. Just above the critical flow speed,
534 Fig. 4(d) shows that the mean value of total work done by the fluid on the
535 plate increases exponentially. The resulting energy transfer is the cause of the
536 instability. However, we again note that it is the fluid-structure interaction
537 in the middle half of the flexible plate that accounts for the overall unstable
538 behaviour. The downstream quarter of the plate is actually doing work on

539 the fluid. The location of destabilising energy transfer leads us to describe the
540 instability under inspection here ($\bar{L} = 1$ and $\bar{H} = 1$) as being *mid-plate-driven*.

541

542 The energy transfers described immediately above arise from the term \dot{W}
543 in the energy equation, Eq. (38). For energy transfer to occur, the product of
544 the terms in the integrand must yield a non-zero result when integrated over
545 a period of oscillation. The time-variations of the terms $(-\delta p)$ and $\dot{\eta}$, in non-
546 dimensional form, are plotted in Fig. 5 for three locations on the flexible plate
547 during the numerical simulation of the critical mode that produced Figs. 4(a)
548 to (c). At early times modal evolution is again seen. For times in the ensuing
549 steady state, the broken lines that we have sketched in connect corresponding
550 peaks in each of the pressure and plate velocity signals for the three locations.
551 These lines serve to illustrate the spatial variation of the phase relationship
552 between these terms. If the pressure and velocity signals were exactly orthog-
553 onal, then there will be no work done over one cycle of oscillation; it is the
554 phase variations to this situation that create the irreversible energy transfers
555 captured in Fig. 4(c) and which underpin the flutter instability represented by
556 Fig. 4(d). The foregoing phase-shifts, away from the orthogonality that would
557 be expected for an infinitely long flexible surface in potential flow, are caused
558 by plate finiteness that combines two effects: those of the leading-edge sin-
559 gularity and the trailing-edge Kutta condition. The relationship between the
560 pressure and velocity at a point on the plate is then uniquely defined by its
561 spatial relationship to the source of these two effects. For one-sided fluid flow
562 over a finite flexible surface, this feature is explained in Lucey and Carpenter
563 (1993a). It will be seen in §3.2 that distancing the leading-edge singularity
564 from the flexible plate through the introduction of an upstream rigid surface
565 causes a significant modification to the plate's response and thus destabilisa-

566 tion occurs through an instability mechanism characteristic of a long plate.
567 This is essentially the same mechanism that was found by Balint and Lucey
568 (2005) for the case of viscous flow destabilising a cantilevered flexible plate
569 through flutter. Finally we remark that the inclusion of material damping
570 leads to a non-zero value of the term \dot{D} in Eq. (38). This subtracts from the
571 rate of energy transfer from fluid flow to the flexible plate and therefore in-
572 creases the value of the critical speed, as seen in Fig. 3(b).

573

574 Results that demonstrate the effect of the mass ratio, \bar{L} , are now presented.
575 Figure 6 shows the variation of system eigenmodes with flow speed for the
576 present case over four decades of \bar{L} (noting that Fig. 6(a) is a reproduction of
577 Fig. 3(a)). Far lower dimensional and non-dimensional critical speeds and oscil-
578 lation frequencies ensue as \bar{L} is increased; this can be seen in the axis labelling
579 in the progression from Fig. 6(a) to Fig. 6(d). In dimensional terms large \bar{L}
580 can represent either a significantly increased fluid loading (for a fixed plate
581 length) or an increased plate length (for a fixed fluid density). Each of these
582 increases the ratio of fluid pressure forces to the opposing restorative forces in
583 the flexible plate (as compared with the dynamics of a short plate near its crit-
584 ical speed). Accordingly, the type of instability that yields the critical speed
585 changes from the single-mode flutter in Fig. 6(a) to a modal-coalescence flutter
586 associated with heavy fluid loading. Thus, in Fig. 6(b) it is clearly the coales-
587 cence of the second and third modes that leads to the ω_R -branch of the second
588 mode turning to enter the positive quadrant. Correspondingly, the ω_R -branch
589 of the third mode dips downwards to give an increasingly damped solution.
590 For elastic plates held at both ends, exact coalescence of the interacting modes
591 occurs to give a complex-conjugate pair of solutions; for example, see Weaver
592 and Unny (1970) and Lucey and Carpenter (1993b). Lucey and Pitman (2006)

593 showed that the introduction of structural damping prevents exact coalescence
 594 in the panel-flutter problem but the system continues to yield what remains
 595 essentially a single-frequency response comprising a highly amplifying and a
 596 highly attenuated pair of roots. Of course, only the amplifying root would
 597 have significance in a physical system. Exact coalescence can occur only in a
 598 wholly conservative system. The present system has been shown to support
 599 non-conservative energy transfers and these act in much the same way as does
 600 the introduction of damping in the panel-flutter problem. Nevertheless the
 601 instability mechanism remains fundamentally of the modal-coalescence type.
 602 With a further increase to $\bar{L} = 100$ in Fig. 6(c), it is again the coalescence of
 603 second and third modes that results in instability. At $\bar{L} = 1000$ in Fig. 6(d),
 604 the coalescence is seen to be more complex involving all of the second, third
 605 and fourth modes. The progression to higher-order *in-vacuo* eigenmodes par-
 606 ticipating in the composition of the critical mode as \bar{L} is increased is clearly
 607 demonstrated in the numerical and experimental results of Yamaguchi *et al.*
 608 (2000a,b) and Watanabe *et al.* (2002a,b).

609

610 Figure 7 shows the results of a numerical simulation for $\bar{L} = 1000$ exactly
 611 at the critical speed ($\bar{U}_c = 1.542 \times 10^{-3}$) found in Fig. 6(d). The plate's mo-
 612 tion can be compared with the corresponding results of the standard case in
 613 Fig. 4. The presence of the higher-order modes predicted by the state-space
 614 calculation is confirmed. This type of modal-coalescence flutter was illustrated
 615 as a travelling-wave form of flutter in Tang and Païdoussis (2007). The pres-
 616 sure loading is now more like that of potential flow over an infinitely long
 617 flexible plate. The magnitude of the pressure due to plate curvature plays the
 618 essential rôle in destabilisation by bringing the two modes to coalescence and
 619 thereby create the phase shift between pressure and plate motion that drives

620 energy into the plate. Thus, instability of the plate now occurs when the flow
621 speed is high enough to produce pressure forces of a sufficient magnitude to
622 modify strongly modal behaviour. As a travelling-wave instability, the insta-
623 bility should be most pronounced over the downstream regions of the plate
624 because these locations are furthest from the leading-edge restraint that in-
625 hibits wave travel. The variation with time of work done by the fluid pressure
626 is shown in Fig. 7(b). The result for the entire flexible plate confirms the state
627 of neutral stability; there is no net transfer of energy between fluid and struc-
628 ture. However, it is also evident that there is energy transmission from fluid
629 to structure over the downstream half and, to a much lesser extent, the first
630 quarter of the flexible plate while the reverse occurs in the second quarter.
631 Thus, the instability that sets in when \bar{U}_c is exceeded can be described as
632 (largely) *downstream-driven*, in contrast to the instability characteristics of a
633 short plate ($\bar{L} = 1$) described earlier.

634

635 A series of numerical experiments to determine the critical flow speeds and
636 associated critical modes within the range of mass ratios $0.2 \leq \bar{L} \leq 1000$
637 has been conducted to compare our results with those of other published
638 work. Watanabe *et al.* (2002b) collected \bar{U}_c data from several theoretical and
639 experimental studies to compare against their own findings. This data has
640 been re-plotted along with our results and is displayed in Fig. 8. The purpose
641 of presenting this figure is two-fold. It gives credence to the validity of our
642 model and it summarises the overall trend of \bar{U}_c -dependence upon \bar{L} for the
643 fluid-structure system. Accordingly, we show only general trends and have not
644 included all of the experimental and theoretical data published to date. For a
645 complete collection of results published to date, the excellent summary figure
646 in Tang and Païdoussis (2007) is recommended. Our values of \bar{U}_c in Fig. 8

647 show good correlation with the other theoretical models. When comparing
648 theory and experiment, it is noted that all models capture the overall trend of
649 the experimental data. As \bar{L} increases the fluid-structure system becomes un-
650 stable at successively lower values of non-dimensional flow speed. All models
651 correctly predict that instabilities above \bar{U}_c are of the flutter type as observed
652 in experiments; we additionally note the point of transition from single-mode
653 flutter to the modal-coalescence type at the bottom of the figure. However,
654 all models fail to capture hysteresis effects found in experiments where several
655 values of \bar{U}_c can be obtained for a single value of \bar{L} . This is most probably
656 due to the existence of a sub-critical instability in the system that cannot be
657 captured by linear models. The large disparity between experimental measure-
658 ments of \bar{U}_c and those theoretically predicted may be due to the omission of
659 three-dimensional effects. The analysis of Eloy *et al.* (2007) modelled trans-
660 verse plane waves on a plate of finite aspect ratio showing that two-dimensional
661 analyses, at infinite aspect ratio, grossly overestimate the pressure loading and
662 thus give unrealistically low critical flow speeds for instability onset. When the
663 finite aspect ratio is taken into account, their Fig. 6 shows that theory and
664 experiment are well-aligned for aspect ratios less than unity. For higher aspect
665 ratios, agreement was less good but, as Eloy *et al.* noted, this may be due to
666 the existence of three-dimensional deflections of the plate in a physical sys-
667 tem. For the related problem of a three-dimensional flexible plate held along
668 each of its edges in one-sided flow, these effects were also reported by Lucey
669 and Carpenter (1993b). Additionally, nearly all of the theoretical models do
670 not model viscous effects explicitly. For large amplitude motions, time-varying
671 separation (upstream of the trailing edge) of the boundary-layer may occur
672 that could create a further type of flutter mechanism.

673

674 Finally, we note from Fig. 8 that our predictions of the dominant eigenmodes
 675 in the form of the critical mode and those of Watanabe *et al.* (2002b) differ
 676 significantly at higher values of \bar{L} . This is because Watanabe *et al.* (2002b)
 677 pre-supposed that the motion of the plate could be made up of the amalga-
 678 mation of the first four *in-vacuo* eigenmodes. In our model there is no such
 679 pre-supposition. As \bar{L} increases the critical mode becomes more complex and
 680 its correspondence to a single *in-vacuo* plate mode becomes increasingly un-
 681 tenable. Our computations capture the fluid-structure eigenmodes directly; at
 682 high \bar{L} these may be very different to those that can be constructed from a lim-
 683 ited set of *in-vacuo* plate modes. Additionally, Figs. 6(a) to (d) show that as \bar{L}
 684 increases, clear changes (or ‘modal switching’) of the critical mode do not oc-
 685 cur. While the single-mode flutter of short plates may be dominated by recog-
 686 nisable *in-vacuo* eigenmodes (principally the second), the modal-coalescence
 687 flutter instability of long plates has been shown to comprise at least two *fluid-*
 688 *loaded* eigenmodes of flexible plate. For long plates the change of critical mode
 689 shape evolves in a continuous manner with \bar{L} .

690 3.2 Variation of Unsteady Model Parameters at $\bar{L} = 1$

691 The fluid-structure dynamics of an effectively isolated ($\bar{H} = 1$) flexible plate
 692 have been elucidated in §3.1 above. We now investigate the effects of includ-
 693 ing additional features in the fluid-structure model for the case of $\bar{L} = 1$.
 694 Thus, we incorporate: a) an unsteady wake, b) channels walls, and c) a rigid
 695 inlet-surface upstream of the flexible plate. Discussion of the results in this
 696 section focuses on how these additional features modify the critical speed and
 697 dynamics of the ‘standard’ $\bar{L} = 1$, $\bar{H} = 1$ case.

698 The effect of including an unsteady wake is illustrated by the results of Fig. 9.
 699 The validation of the linearised, discrete-vortex method and its coupling with
 700 a fixed-geometry boundary-element method is presented in Howell (2006). The
 701 effect of the shed vorticity increases the critical speed, \bar{U}_c (for the standard
 702 case $\bar{L} = 1$, $\bar{H} = 1$) from 5.452 to 5.948, an increase of approximately 9%.
 703 The shed vorticity increases the magnitude of the fluid pressure near the trail-
 704 ing edge due to the terms \dot{u}^{Nb} and u^{Nb} in Eq. (19). The wider neck of the
 705 mode shape seen in Fig. 9(a), as compared with that of Fig. 4(a), indicates
 706 an increased component of lower-order modes; this is borne out by an oscilla-
 707 tion frequency, $\bar{\omega}$, of 0.61 as compared with 0.69 for the standard case. These
 708 changes are consistent with the increased pressure loading near the trailing
 709 edge of the plate when the wake effects are included.

710

711 At first sight, an increased magnitude of the fluid pressure near the trailing
 712 edge might seem incompatible with stabilisation as evidenced by the increase
 713 in critical speed. However, we recall that the single-mode flutter of this short
 714 plate arises not from the magnitude of the pressure force but from its phase
 715 relationship with the plate's motion. Because the wake is a periodic contin-
 716 uation of the bound vorticity, it exercises an effect that is similar to that of
 717 increased plate length on the phase relation between the pressure acting on
 718 the plate and its velocity. Thus, the pressure and velocity signals are closer
 719 to being orthogonal when the wake is included and this reduces the potency
 720 of the phase-shift mechanism of the single-mode flutter of short plates. How-
 721 ever, its inclusion does not eliminate single-mode flutter (nor replace it with
 722 modal-coalescence flutter as would increasing plate length). The modification
 723 of the phase between pressure and plate velocity, effected by the wake, reduces
 724 the rate of energy transfers between fluid flow and structure and this leads

725 to an increase in the critical speed for short plates. This is demonstrated by
726 Fig. 9(b) in which we have plotted the energy transfers for each of the four
727 quarters of the plate with and without the wake included. The flow is at the
728 critical speed $\bar{U} = 5.452$ that is obtained without a wake and thus the mean
729 value of the total \bar{W} for the wake results is marginally decreasing thereby
730 indicating an attenuating response at this flow speed. As would be expected
731 the greatest reductions in the energy-transfer mechanism are seen to occur in
732 the third and fourth quarters of the flexible plate that are most strongly influ-
733 enced by the wake vorticity. Table 1 lists the values of the critical speed with,
734 \bar{U}_c^* , and without, \bar{U}_c , the wake effects, along with the proportional difference
735 $(\bar{U}_c^* - \bar{U}_c)/\bar{U}_c$, for a range of \bar{L} . This data corroborates the discussion above by
736 demonstrating that wake effects are stabilising for short plates. Longer plates
737 are less affected by the wake but experience a destabilising effect because they
738 succumb to modal-coalescence flutter that results from the pressure and plate
739 velocity signals being more closely orthogonal.

740

741 The effect of a rigid central surface, equal in length to the flexible surface,
742 placed upstream of the flexible surface and in the effective absence of channel
743 walls ($\bar{H} = 1$) is now investigated. Figure 10 maps the variation of system
744 eigenmodes with flow speed for the present case and can be contrasted with
745 Fig. 3(a); similarly, Figs. 11(a) and (b) show the critical mode and energy
746 transfer from fluid to structure respectively and can be compared with the
747 corresponding results of the standard case in Figs. 4(a) and (c). We note that
748 the third mode (marked 3) of the fluid-structure system is the first to become
749 unstable, $\bar{\omega}_R > 0$ for $\bar{U} > \bar{U}_c = 13.547$. The critical speed is substantially
750 higher than $\bar{U}_c = 5.452$ found in the absence of a rigid central surface. The in-
751 clusion of the rigid central surface stabilises the second-mode flutter that was

752 previously critical. That single-mode flutter was shown to be caused by the
 753 phase relationship between fluid pressure and plate velocity that can be at-
 754 tributed in part to the effect of high flow curvature caused by the leading-edge
 755 singularity. The introduction of a rigid central-surface moves the singularity
 756 much further upstream of the flexible plate and that destabilisation mecha-
 757 nism is diminished. The principal instability mechanism is now seen in Fig. 10
 758 to be a modal-coalescence of Modes 2 and 3 and this is clearly reflected in
 759 the mode shape of Fig. 11(a). Thus, the flexible plate behaves in a way that
 760 is closer to that of a plate with high \bar{L} - see Figs. 6 and 7. This then sug-
 761 gests that the effect of an upstream rigid plate of fixed length decreases as \bar{L}
 762 is increased, a result that was shown by Tang and Païdoussis (2007). What
 763 is perhaps surprising in the present results is that the greatest destabilising
 764 energy transfer continues to occur in the middle half of the plate as shown in
 765 Fig. 11(b), even though the instability is now essentially a modal-coalescence
 766 flutter.

767

768 The effect of channel walls is now investigated. These are placed at a dis-
 769 tance of one-tenth of the plate length from the plate and thus $\bar{H} = 0.1$. Plots
 770 of the critical mode and the energy-transfer from fluid to wall are presented
 771 in Fig. 12. The proximity of the walls when $\bar{L} = 1$ reduces \bar{U}_c by 5% rela-
 772 tive to the isolated case. This configuration in which channel-wall proximity
 773 affects the behaviour and stability of the flexible plate has been studied by
 774 Aurégan and Depollier (1995) and Guo and Païdoussis (2000). The lowering
 775 of \bar{U}_c , relative to the isolated case, is caused by an increase in the pressure dif-
 776 ference across the plate that occurs through mass-conservation and Bernoulli
 777 effects in a channel of finite width. This supplements the pressure difference
 778 caused by plate curvature and motion, the only sources of pressure difference

779 when channel walls are absent. However, the channel walls do not significantly
780 modify the location of the greatest amount of fluid work done on the plate;
781 see Fig. 12(b). Like the standard case of §3.1, energy transfer from fluid to
782 structure occurs in the second and third quarters of the plate while the reverse
783 occurs in the downstream quarter. Accordingly we can continue to describe
784 the destabilisation as being *mid-plate-driven*. The effect of the channel walls
785 is also seen in the form of the critical mode plotted in Fig. 12(a) that has
786 both a wider neck and higher amplitude (relative to the same form of initial
787 excitation) as compared to its counterpart in Fig. 4(a).

788 3.3 Potential Snores

789 The computational model is now used to study a particular application of
790 the foregoing fluid-structure interactions. In doing so, however, we are able to
791 illustrate the general effects of time-varying mean flow and inhomogeneity in
792 the properties of the flexible plate. The geometry shown in Fig. 1 is assumed
793 to be an approximation of the human pharynx: the channel walls represent the
794 throat, a rigid-inlet the hard palate and the flexible plate is the soft palate.
795 We are therefore able to model the basic features of human snoring where such
796 snores are directly related to flutter of the soft palate. Similar approaches to
797 modelling human snoring have been made by Gavriely and Jensen (1993),
798 Aurégan and Depollier (1995), Huang (1995), Balint and Lucey (2005) and
799 Tetlow *et al.* (2006). Appropriate non-dimensional parameters based on hu-
800 man dimensions are $\bar{L} = 0.42$ and $\bar{H} = 0.1$. It is assumed a snore is initiated
801 when the oscillation of the plate becomes unstable, *i.e.* above \bar{U}_c .

802

803 We first study the effect of using a time-varying mean flow $\bar{U}(\bar{t})$ that approxi-
 804 mately models inhalation during sleep. The inhalation lasts for one second (or
 805 4.28 units of non-dimensional time), during which time \bar{U} increases linearly
 806 from zero to a chosen maximum velocity. Therefore, a *velocity gradient* exists;
 807 this is the maximum velocity gradient for which the flexible surface is still
 808 stable at the end of the ‘inhalation’. The development of the critical mode is
 809 illustrated in Fig. 13(a) that shows a series of instantaneous deflections of the
 810 flexible plate between the times $\bar{t} = 4.24$ and 4.28. The run commenced at
 811 $\bar{t} = 0$ with the plate’s second *in-vacuo* mode applied as an initial deflection;
 812 this is also plotted in Fig. 13(a). The applied initial deflection decays but from
 813 it emerges a higher-order system mode of the type promoted by increased fluid
 814 loading in §3.1 and the inclusion of an upstream rigid surface in §3.2. This is
 815 evident first in the appearance of the envelope of deflections seen in Fig. 13(a)
 816 that is formed at times for which $\bar{U}(\bar{t})$ is close to those which yield neutral
 817 stability. However, because the flow speed continues to increase to its maxi-
 818 mum applied value at $\bar{U}(4.28)$, strong amplification is then seen in the series of
 819 final instantaneous deflections. The emergence of a higher-order mode as that
 820 which destabilises the system suggests a modal-coalescence flutter mechanism
 821 that we have shown earlier to be promoted by increasing fluid loading or plate
 822 length for a steady applied flow. In the present case the increased fluid loading
 823 arises from a much higher final flow speed, $\bar{U} = 41.8$, at $\bar{t} = 4.28$ (3.7 m/s after
 824 1 second), than would have been required to destabilise the second mode had
 825 a steady flow speed of $\bar{U} = 26.5$ (2.34 m/s) been applied. Figure 13(b) shows
 826 the associated time-variation of fluid work done \bar{W} over the period that culmi-
 827 nates in the end of inhalation for the critical velocity gradient. It is clear that
 828 the instability is driven by the fluid work done on the third, second and first
 829 quarters of the plate in order of the magnitude of contribution to the plate’s

830 destabilisation. Figure 14 shows the time-variation of flexible-surface velocity
 831 and fluid pressure over the same time period as plotted in Fig. 13(b). At the
 832 location $\bar{x} = 0.7$ in Fig. 14(c) that resides within the third quarter where
 833 the greatest destabilising work occurs, it is seen that $(-\bar{\delta p})$ and $\bar{\eta}$ are almost
 834 in-phase. This provides further evidence for characterising the instability as
 835 being of the modal-coalescence type since exact phase alignment indicates a
 836 pure resonance of fluid loading and plate motion. Finally, we recognise that
 837 the critical velocity gradient found is specific to the initial excitation applied.
 838 As evident from Fig. 13(a), we applied the second *in-vacuo* mode that might
 839 have been expected to promote flutter of the second system mode. What we
 840 therefore emphasise is that the single-mode flutter mechanism that has been
 841 seen to be the critical instability for short plates in steady uniform flow may
 842 not establish itself in a time-varying mean flow. Thus, the critical instability
 843 is likely to be the more robust modal-coalescence instability that typically
 844 occurs at higher mean-flow dynamic pressures.

845

846 We now briefly investigate the effect of spatially varying plate stiffness for
 847 the case of uniform mean flow. The critical speed for a homogeneous flexible
 848 plate in a system with $\bar{L} = 0.42$ and $\bar{H} = 0.1$ is first found. The evaluation
 849 of \bar{W} , see Fig. 15(a), indicates that the instability causing this snore is driven
 850 solely by energy transfer on the third quarter of the plate, the characteristic
 851 similar to that seen in Fig. 12(b) ($\bar{L} = 1$, $\bar{H} = 0.1$) but with no assistance from
 852 the second quarter of the plate. The plate energy, \bar{E}_t , for this case is shown in
 853 Fig. 15(b) and is seen to maintain a constant mean value appropriate to the
 854 neutrally-stable state of the plate. We then mimic a proposed ‘cure’ for the
 855 snore by applying a 10% greater stiffness in the third quarter of the flexible
 856 surface where the instability mechanism occurs. This soft-palate stiffening is a

857 strategy similar to that described by Ellis *et al.* (1993). The resulting trace of
858 plate energy is shown in Fig. 15(c) and the strategy is indeed found to have a
859 stabilising effect. If the same simulated stiffening is applied to the first quar-
860 ter of the flexible plate instead of the third quarter, the result of Fig. 15(d)
861 shows that the change is actually destabilising. These results demonstrate that
862 flexible-plate stiffening can be used to control stability for the alleviation of
863 palatal snoring but that the location of such stiffening is critical in order to
864 achieve the desired effects.

865 4 Conclusions

866 We have developed and deployed a new computational model for the fluid-
867 structure interaction between a cantilevered-free flexible plate and an ideal
868 flow. The model permits numerical simulations to be conducted that capture
869 transient behaviour and in which spatially localised fluid-structure interactions
870 can be identified. The computational model can also be used to determine the
871 global stability of the system for the infinite-time limit. Using these solution
872 methods in combination we have elucidated instability mechanisms showing
873 how spatially varying fluid-structure interactions along the plate combine to
874 give the system response.

875

876 The investigations presented in this paper provide an accurate linear-stability
877 map for the standard case of cantilevered-free flexible plate in an unbounded
878 uniform flow. We have then investigated the changes to this ‘standard’ fluid-
879 structure interaction that are caused by the effects of: a) shed vorticity, b)
880 channel walls, c) a rigid inlet-surface, d) temporally-varying inlet flow-velocity,

881 and e) variable plate stiffness. A summary of the effects of (a)-(c) is given in
882 Table 2. Overall, we can conclude that short flexible plates are destabilised
883 by single-mode flutter caused by an irreversible energy transfer from fluid to
884 structure that principally occurs over the middle part of the flexible plate.
885 In contrast, long flexible plates succumb to a modal-coalescence flutter that
886 is principally driven by the magnitude of the fluid loading as opposed to
887 the subtle phase relationships that underpin single-mode flutter. Thus, the
888 modal-coalescence flutter has its parallel in the Kelvin-Helmholtz instability
889 of flexible plates held at both ends at flow speeds higher than those that give
890 divergence instability. The proximity of channel walls tends to intensify the
891 single-mode flutter mechanism whereas the inclusion of a rigid inlet surface
892 diminishes the mechanism so that a higher critical flow speed associated with
893 modal-coalescence is reached before instability sets in. The effect of a wake is
894 to decrease the potency of the single-mode flutter mechanism that dominates
895 the destabilisation of short plates with light fluid loading and thereby increase
896 critical speeds. However, wake effects promote the modal-coalescence flutter
897 that is the critical instability for long plates or those with heavy fluid loading
898 and are therefore destabilising; the magnitude of this effect reduces with in-
899 creases to plate length.

900

901 By elucidating the instability mechanisms to which the fluid-structure sys-
902 tem is prone, we have identified two distinct types of plate flutter. While the
903 energy flow between fluid and structure for both is caused by phase-shifts be-
904 tween the pressure load and the motion of the plate, the mechanics behind
905 the phase shifts are very different. This has implications for the engineering
906 control (or exploitation) of the instabilities. Structural forces are dominant in
907 the single-mode flutter of short plates and it is the phase-relationship (to plate

908 motion), as opposed to the magnitude, of the fluid pressure that is critical.
909 Thus, this instability, as we have shown, can be controlled by the judicious
910 stiffening of parts of the plate or the inclusion of damping, for example, by
911 doping the plate material. In contrast, the appearance of the destabilising
912 phase shift in modal-coalescence flutter is principally dependent of the mag-
913 nitude of the pressure load that brings the coalescing modes together. Thus,
914 damping has only a mildly modifying effect on the critical speed. Localised
915 stiffening strategies, as a means to design out the instability, would also be
916 difficult to implement. The added stiffness would need to be applied in such a
917 way that it separated out the principal modes in the frequency space in order
918 to postpone their coalescence with increasing flow speed.

919

920 The effects of time-varying mean flow and of spatially varying flexible-plate
921 properties have been illustrated in the context of upper-airway dynamics and
922 the mechanisms that might lie behind palatal snoring. We have shown that
923 stiffening does have the potential to increase the critical speed of palatal flut-
924 ter provided that it is applied in the correct location. This highlights the
925 difficulty of applying successful treatment to a patient suffering from palatal
926 snoring. This difficulty is compounded by the potential existence of two dif-
927 ferent types of instability that we have highlighted in this paper. Increasing
928 complexity occurs when a more faithful representation of the upper airway is
929 modelled. Aurégan and Depollier (1995) introduced two broad classifications
930 namely, *pure* and *apnœic* snores, owing to the flexibility of the soft palate and
931 channel properties respectively. Moreover, the site of snore generation is not
932 necessarily confined to the region of the soft-palate but to various sites in the
933 human pharynx, as shown by Miyazaki *et al.* (1998). It therefore follows that
934 there will be different treatments for each type of snore and that treatment

935 must be tailored to the individual patient. Fundamental understanding of the
936 fluid-structure interactions at work undoubtedly will underpin the appropriate
937 developments of such treatments.

938 **5 Acknowledgements**

939 Much of the work described in this paper was carried out while R.M.H. was in
940 receipt of an EPSRC grant at the University of Warwick and during periods
941 as a visiting academic hosted by Curtin University of Technology.

942 **References**

- 943 Argentina, M. & Mahadevan, L. 2005 Fluid-flow-induced flutter of a flag.
944 *Proceedings of the National Academy of Sciences of the United States of*
945 *America* **102**(6):1829-1834.
- 946 Aurégan, Y. & Depollier, C. 1995 Snoring: Linear stability analysis and *in*
947 *vitro* experiments. *Journal of Sound and Vibration* **188**(1):39-54.
- 948 Balint, T. S. & Lucey, A. D. 2005 Instability of a cantilevered flexible plate in
949 viscous channel flow. *Journal of Fluids and Structures* **20**(7):893-912.
- 950 Carpenter, P. W. & Garrad, A. D. 1985 The hydrodynamic stability of flow
951 over Kramer-type compliant surfaces. Part 1. Tollmien-Schlichting instabil-
952 ities. *Journal of Fluid Mechanics* **155**:465-510.
- 953 Chorin, A. J. 1973 Numerical study of slightly viscous flow. *Journal of Fluid*
954 *Mechanics* **57**(4):785-796.
- 955 Crighton, D. G. & Oswell, J. E. 1991 Fluid loading with mean flow. I. Response

- 956 of an elastic plate to localized excitation. *Philosophical Transactions of the*
957 *Royal Society of London A* **335**:557-592.
- 958 Doaré, O. & de Langre, E. 2002 Local and global instability of fluid-conveying
959 pipes on elastic foundations. *Journal of Fluids and Structures* **16**(1): 1-14.
- 960 Doaré, O. & de Langre, E. 2006 The role of boundary conditions in the in-
961 stability of one-dimensional systems. *European Journal Mechanics B/Fluids*
962 **25**: 948-959.
- 963 Ellis, P. D. M., Ffowcs Williams, J. E. & Shneerson, J. M. 1993 Surgical relief
964 of snoring due to palatal flutter: A preliminary report. *Annals of the Royal*
965 *College of Surgeons of England* **75**:286-290.
- 966 Eloy, C., Souilliez, C. & Schouveiler, L. 2007 Flutter of a rectangular can-
967 tilevered plate. *Journal of Fluids and Structures* **23**(6):904-919.
- 968 Gavriely, N. & Jensen, O. 1993 Theory and measurement of snores. *Journal*
969 *of Applied Physiology* **74**(6):2828-2837.
- 970 Guo, C. Q. & Païdoussis, M. P. 2000 Stability of rectangular plates with
971 free side-edges in two-dimensional inviscid channel flow. *Journal of Applied*
972 *Mechanics* **67**:171-176.
- 973 Howell, R. M., Lucey, A. D. & Carpenter, P. W. 2004 Numerical simulation
974 of a cantilevered flexible plate embedded in an unbounded inviscid flow. In
975 *Proceedings of the 8th international conference on Flow-Induced Vibrations,*
976 *Paris, France* (edited by F. Axisa and E. de Langre), pp:167-171.
- 977 Howell, R. M. 2006 Snoring: A flow-structure interaction. Ph.D Thesis, Uni-
978 versity of Warwick.
- 979 Huang, L. 1995 Flutter of cantilevered plates in axial flow. *Journal of Fluids*
980 *and Structures* **9**:127-147.
- 981 Kornecki, A., Dowell, E. H. & O'Brien, J. 1976 On the aeroelastic instability
982 of two-dimensional panels in uniform incompressible flow. *Journal of Sound*

- 983 *and Vibration* **47**(2):163-178.
- 984 Lucey, A.D. & Carpenter, P.W. 1992 A numerical simulation of the interaction
985 of a compliant wall and inviscid flow. *Journal of Fluid Mechanics* **234**:121-
986 146.
- 987 Lucey, A. D. & Carpenter, P. W. 1993a On the difference between the hy-
988 droelastic instability of infinite and very long compliant panels. *Journal of*
989 *Sound and Vibration* **163**(1):176-181.
- 990 Lucey, A.D. & Carpenter, P.W. 1993b The hydroelastic stability of three-
991 dimensional disturbances of a finite compliant panel. *Journal of Sound and*
992 *Vibration* **165**:527-552.
- 993 Lucey, A. D, Cafolla, G. J. & Carpenter, P. W. 1998 The effect of a boundary
994 layer on the hydroelastic stability of a flexible wall. In *Proceedings of the 3rd*
995 *International Conference on Engineering Hydroelasticity*, J. Horacek and I.
996 Zolotarev, eds., Czech Technical University Press, pp. 268-273.
- 997 Lucey, A. D. & Pitman, M. W. 2006 A new method for determining the eigen-
998 modes of finite flow-structure systems. In *Proceedings of ASME Pressure*
999 *Vessels and Piping Division Conference, Vancouver, BC, Canada* Paper
1000 no.: PVP2006-ICPVT11-93940.
- 1001 Miyazaki, S., Itasaka, Y., Ishikawa, K. & Togawa, K. 1998 Acoustic analysis
1002 of snoring and the site of airway obstruction in sleep related respiratory
1003 disorders. *Acta Oto-Laryngologica* **118**(Supplement 537):47-51.
- 1004 Tang, L. & Païdoussis, M. P. 2006 A numerical investigation on the dynamics
1005 of two-dimensional cantilevered flexible plates in axial flow. In *Proceedings*
1006 *of ASME Pressure Vessels and Piping Division Conference, Vancouver, BC,*
1007 *Canada* Paper no.: PVP2006-ICPVT11-93817.
- 1008 Tang, L. & Païdoussis, M. P. 2007 On the instability and the post-critical be-
1009 haviour of two-dimensional cantilevered flexible plates in axial flow. *Journal*

1010 *of Sound & Vibration* **305**:97-115.

1011 Tetlow, G.A., Lucey A.D. & Balint, T.S. 2006 Instability of a cantilevered
1012 flexible plate in viscous channel flow driven by constant pressure drop.
1013 In *Proceedings of ASME Pressure Vessels and Piping Division Conference*,
1014 *Vancouver, BC, Canada* Paper no.: PVP2006-ICPVT11-93943.

1015 Watanabe, Y., Suzuki, S., Sugihara, M. & Sueoka, Y. 2002a An experimental
1016 study of paper flutter. *Journal of Fluids and Structures* **16**(4):529-542.

1017 Watanabe, Y., Isogai, K., Suzuki, S. & Sugihara, M. 2002b A theoretical study
1018 of paper flutter. *Journal of Fluids and Structures* **16**(4):543-560.

1019 Weaver, D. S. & Unny, T. E. 1970 The hydroelastic stability of a flat plate.
1020 *ASME, Journal of Applied Mechanics* **37**(1):823-827.

1021 Yamaguchi, N., Yokota, K. & Tsujimoto, Y. 2000a Flutter limits and be-
1022 haviours of a flexible thin sheet in high speed flow - I: Analytical method
1023 for prediction of the sheet behaviour. *Journal of Fluids Engineering* **122**:65-
1024 73.

1025 Yamaguchi, N., Sekiguchi, T., Yokota, K. & Tsujimoto, Y. 2000b Flutter limits
1026 and behaviours of a flexible thin sheet in high speed flow - II: Experimen-
1027 tal results and predicted behaviours for low mass ratios. *Journal of Fluids*
1028 *Engineering* **122**:74-83.

1029 **List of Tables**

1030

1031 Table 1. Effect of an unsteady wake on the critical velocity: Variation of the
1032 critical velocity, \bar{U}_c , with \bar{L} ; \bar{U}_c^* is the critical velocity when the unsteady wake
1033 effect is included.

1034

1035 Table 2. Summary of flutter instability dependence upon system configura-
1036 tion.

1037

1038 **List of Figures**

1039

1040 Figure 1. Schematic of the fluid-structure system studied.

1041

1042 Figure 2. Fluid-structure system: Diagrammatic representation of the com-
1043 putational methods used and the system discretisation.

1044

1045 Figure 3. Fluid-structure behaviour at $\bar{L} = 1$, $\bar{H} = 1$ (effectively isolated):
1046 Variation of system eigenmodes with flow speed where (a) elastic plate, $\bar{d} = 0$,
1047 and (b) including structural damping with $\bar{d} = 5$. The numbers on each figure
1048 identify the mode number in order of ascending frequency at $\bar{U} = 0$.

1049

1050 Figure 4. Fluid-structure behaviour at $\bar{L} = 1$, $\bar{H} = 1$ (effectively isolated):
1051 Numerical simulations of system behaviour with $\bar{d} = 0$ at the critical flow
1052 speed $\bar{U}_c = 5.452$, (a) time-sequence of instantaneous plate deformation (the
1053 thick line is the initially imposed deformation), (b) time-variation of plate
1054 energy, \bar{E}_t , (c) time-variation of work done by fluid on plate, \bar{W} , and, for a
1055 post-critical flow speed $\bar{U} = 6.0$, (d) time-variation of work done by fluid on

1056 plate, \bar{W} . In both (c) and (d) the lines — (thin), $-\circ-$, $-\bullet-$ and \cdots respectively
 1057 indicate the work done over the first, second, third and fourth quarters of the
 1058 plate from its leading edge while — (thick) is the sum of these contributions.

1059

1060 Figure 5. Fluid-structure behaviour at $\bar{L} = 1$, $\bar{H} = 1$ (effectively isolated):
 1061 Variation of perturbation pressure, $-\bar{\delta p}$ (denoted \circ), and plate velocity, $\bar{\eta}$ (de-
 1062 noted $*$) with time at (a) $\bar{x} = 0.3$, (b) $\bar{x} = 0.5$, and $\bar{x} = 0.7$ for the numerical
 1063 simulation that yielded Figs 4(a), 4(b) and 4(c) at the critical flow speed.
 1064 The added lines ——— and — — — respectively connect peaks of $-\bar{\delta p}$ and $\bar{\eta}$ to
 1065 illustrate the spatial variation of the phase between these terms.

1066

1067 Figure 6. Fluid-structure behaviour for various \bar{L} at $\bar{H} = 1$ (effectively iso-
 1068 lated): Variation of system eigenmodes with flow speed for $\bar{d} = 0$ for (a) $\bar{L} = 1$
 1069 (as in Fig. 3(a)), (b) $\bar{L} = 10$, (c) $\bar{L} = 100$, and (d) $\bar{L} = 1000$. The numbers on
 1070 each figure identify the mode number in order of ascending frequency at $\bar{U} = 0$.

1071

1072 Figure 7. Fluid-structure behaviour at $\bar{L} = 1000$, $\bar{H} = 1$ (effectively iso-
 1073 lated): Numerical simulations of system behaviour with $\bar{d} = 0$ at the critical
 1074 flow speed $\bar{U} = U_c = 1.542 \times 10^{-3}$, (a) time-sequence of instantaneous plate
 1075 deformation (the thick line is the initially imposed deformation), and (b) time-
 1076 variation of work done by fluid on plate, \bar{W} , in which — (thin), $-\circ-$, $-\bullet-$ and
 1077 \cdots respectively indicate the work done over the first, second, third and fourth
 1078 quarters of the plate from its leading edge while — (thick) is the sum of these
 1079 contributions.

1080

1081 Figure 8. Fluid-structure behaviour for a range of \bar{L} at $\bar{H} = 1$ (effectively
 1082 isolated): Plot of U_c at different \bar{L} (adapted from Watanabe *et al.* (2002b)).

1083 Data is from several published studies. Experimental Data: From Watanabe
 1084 *et al.* (2002b) \circ flag type paper, \bullet long-type paper, \triangle elastic sheet; \diamond Huang
 1085 (1995); $+$ Kornecki *et al.* (1976); Theoretical Models: \square Kornecki *et al.* (1976);
 1086 $-$ (thin) Huang (1995); $-$ (thick) Guo and Païdoussis (2000); $-\cdot$ Watanabe *et*
 1087 *al.* (2002b) with their parameter $C_D = 0$; $--$ Present theory. The first set of
 1088 boundaries at the bottom of the graph show the predominant *in vacuo* eigen-
 1089 mode in the form of the critical mode calculated by the theoretical model of
 1090 Watanabe *et al.* (2002b); the second set of boundaries are from our numer-
 1091 ical simulations, also showing the predominant eigenmode when the flutter
 1092 instability predicted is of the single-mode type, but also showing which group
 1093 of modes form the critical mode when the flutter instability is of the modal-
 1094 coalescence type.

1095

1096 Figure 9. The effect of an unsteady wake on the system response: Numeri-
 1097 cal simulations of system behaviour at $\bar{L} = 1$, $\bar{H} = 1$ (effectively isolated) and
 1098 $\bar{d} = 0$, (a) time-sequence of instantaneous plate deformation at the new criti-
 1099 cal flow speed $\bar{U}_c = 5.948$ (the thick line is the initially imposed deformation
 1100 and note that early deformations have been removed to provide a clearer view
 1101 of the critical mode), and (b) time-variation of work done by fluid on plate,
 1102 \bar{W} , with (discrete data) and without (continuous data) a wake at $\bar{U}_c = 5.452$
 1103 (the critical speed found without a wake) where the data sequences \triangle , $+$, \diamond ,
 1104 \times and $—$ (thin), $-\circ-$, $-\bullet-$, \dots each respectively indicate the work done over
 1105 the first, second, third and fourth quarters of the plate from its leading edge,
 1106 while \square and $—$ (thick) are the respective sums of these contributions.

1107

1108 Figure 10. The effect of an upstream, rigid central-surface on the system re-
 1109 sponse: Variation of system eigenmodes with flow speed for $\bar{L} = 1$, $\bar{H} = 1$

1110 (effectively isolated) and $\bar{d} = 0$ when an upstream, rigid central-surface (equal
1111 in length to the flexible plate) is introduced. The numbers on each figure iden-
1112 tify the mode number in order of ascending frequency at $\bar{U} = 0$.

1113

1114 Figure 11. The effect of an upstream, rigid central-surface on the system
1115 response: Numerical simulation of system behaviour for $\bar{L} = 1$, $\bar{H} = 1$ (ef-
1116 fectively isolated) and $\bar{d} = 0$ at the new critical flow speed $\bar{U}_c = 13.547$, (a)
1117 time-sequence of instantaneous plate deformation (the thick line is the initially
1118 imposed deformation), and (b) time-variation of work done by fluid on plate,
1119 \bar{W} , in which — (thin), $-\ominus-$, $-\bullet-$ and \cdots respectively indicate the work done
1120 over the first, second, third and fourth quarters of the plate from its leading
1121 edge while — (thick) is the sum of these contributions.

1122

1123 Figure 12. The effect of channel walls on the system response: Numerical sim-
1124 ulation of system behaviour for $\bar{L} = 1$, $\bar{H} = 0.1$ and $\bar{d} = 0$ at the new critical
1125 flow speed $\bar{U}_c = 5.177$, (a) time-sequence of instantaneous plate deformation
1126 (the thick line is the initially imposed deformation), and (b) time-variation of
1127 work done by fluid on plate, \bar{W} , in which — (thin), $-\ominus-$, $-\bullet-$ and \cdots respec-
1128 tively indicate the work done over the first, second, third and fourth quarters
1129 of the plate from its leading edge while — (thick) is the sum of these contri-
1130 butions.

1131

1132 Figure 13. The effect of time-varying uniform flow on the system response:
1133 Numerical simulation of system behaviour for $\bar{L} = 0.42$, $\bar{H} = 0.1$ (these di-
1134 mensions mimicking that of the human upper airway) and $\bar{d} = 0$ with an
1135 upstream rigid central surface (equal in length to the flexible plate) present,
1136 (a) time-sequence of instantaneous plate deformation (the thick line is the ini-

1137 tially imposed deformation while \diamond and \ominus denote deformations at $\bar{t} = 4.24$
1138 and 4.28 respectively, and deformations prior to this time period have been
1139 removed to provide a clearer view of the critical mode that develops), and (b)
1140 time-variation of work done by fluid on plate, \bar{W} , in which — (thin), \ominus ,
1141 \bullet and \cdots respectively indicate the work done over the first, second, third
1142 and fourth quarters of the plate from its leading edge while — (thick) is
1143 the sum of these contributions. $\bar{U}(\bar{t})$ increases from 0 to 41.8 over the period
1144 $\bar{t} : 0 \rightarrow 4.28$.

1145

1146 Figure 14. The effect of time-varying uniform flow on the system response:
1147 Variation of perturbation pressure, $-\bar{\delta p}$ (dashed line), and plate velocity, $\bar{\eta}$
1148 (continuous line) with time at (a) $\bar{x} = 0.3$, (b) $\bar{x} = 0.5$, and $\bar{x} = 0.7$ for the
1149 numerical simulation that yielded Fig. 13.

1150

1151 Figure 15. The effect of spatially varying plate stiffness on the system re-
1152 sponse: Numerical simulation of system behaviour for $\bar{L} = 0.42$, $\bar{H} = 0.1$
1153 (these dimensions mimicking that of the human upper airway) and $\bar{d} = 0$
1154 with an upstream rigid central surface (equal in length to the flexible plate)
1155 present, (a) homogeneous flexible plate at its critical flow speed $\bar{U}_c = 26.5$:
1156 time-variation of work done by fluid on plate, \bar{W} , in which — (thin), \ominus , \bullet
1157 and \cdots respectively indicate the work done over the first, second, third and
1158 fourth quarters of the plate from its leading edge while — (thick) is the sum
1159 of these contributions, and variation of plate energy with time at $\bar{U} = 26.5$ for
1160 (b) homogeneous flexible plate, (c) flexible plate with a 10% increase in plate
1161 stiffness over its third quarter, and (d) flexible plate with a 10% increase in
1162 plate stiffness over its first quarter.

\bar{L}	\bar{U}_c	\bar{U}_c^*	$(\bar{U}_c^* - \bar{U}_c)/\bar{U}_c$
0.2	40.2000	54.3800	0.35
0.6	9.6400	11.4700	0.19
1.0	5.4520	5.9480	0.09
1.2	4.5846	4.7269	0.03
1.4	4.0123	3.9533	-0.01
1.6	3.6312	3.4385	-0.05

Tab. 1.

Simulation Description	\bar{L}	\bar{H}	% change in U_c from 'standard' case	$\bar{\omega}$	Region of plate where most destabilising energy transfer occurs	(Incipient) Flutter type
Standard	1	1 ($=\infty$)	—	0.69	Middle half	Single-mode
Long plate/heavy fluid loading	1000	1 ($=\infty$)	-99.97%	0.19	Mainly downstream half	Modal-coalescence
Wake included	1	1 ($=\infty$)	9.10%	0.61	Middle half	Single-mode
Rigid, upstream central-surface	1	1 ($=\infty$)	148.48%	1.64	Middle half	Modal-coalescence
Channel flow	1	0.1	-5.04%	0.63	Middle half	Single-mode

Tab. 2.

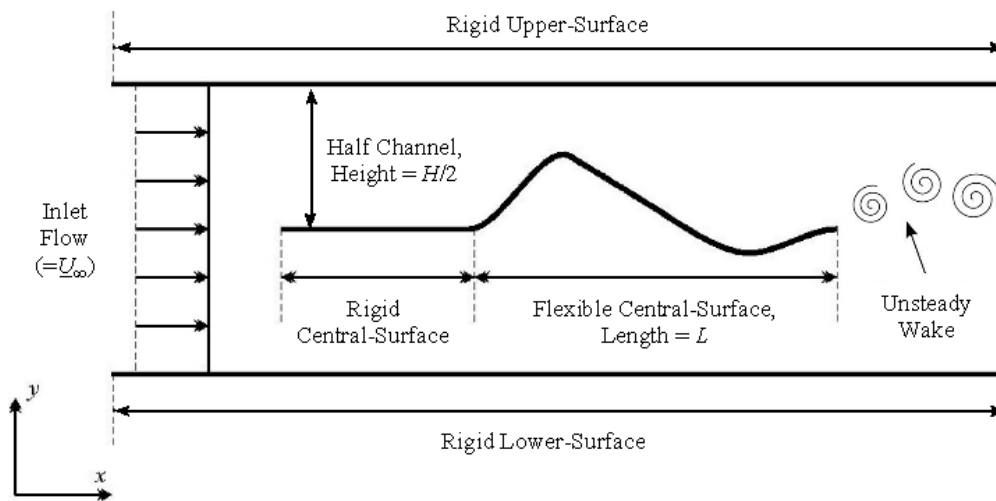


Fig. 1.

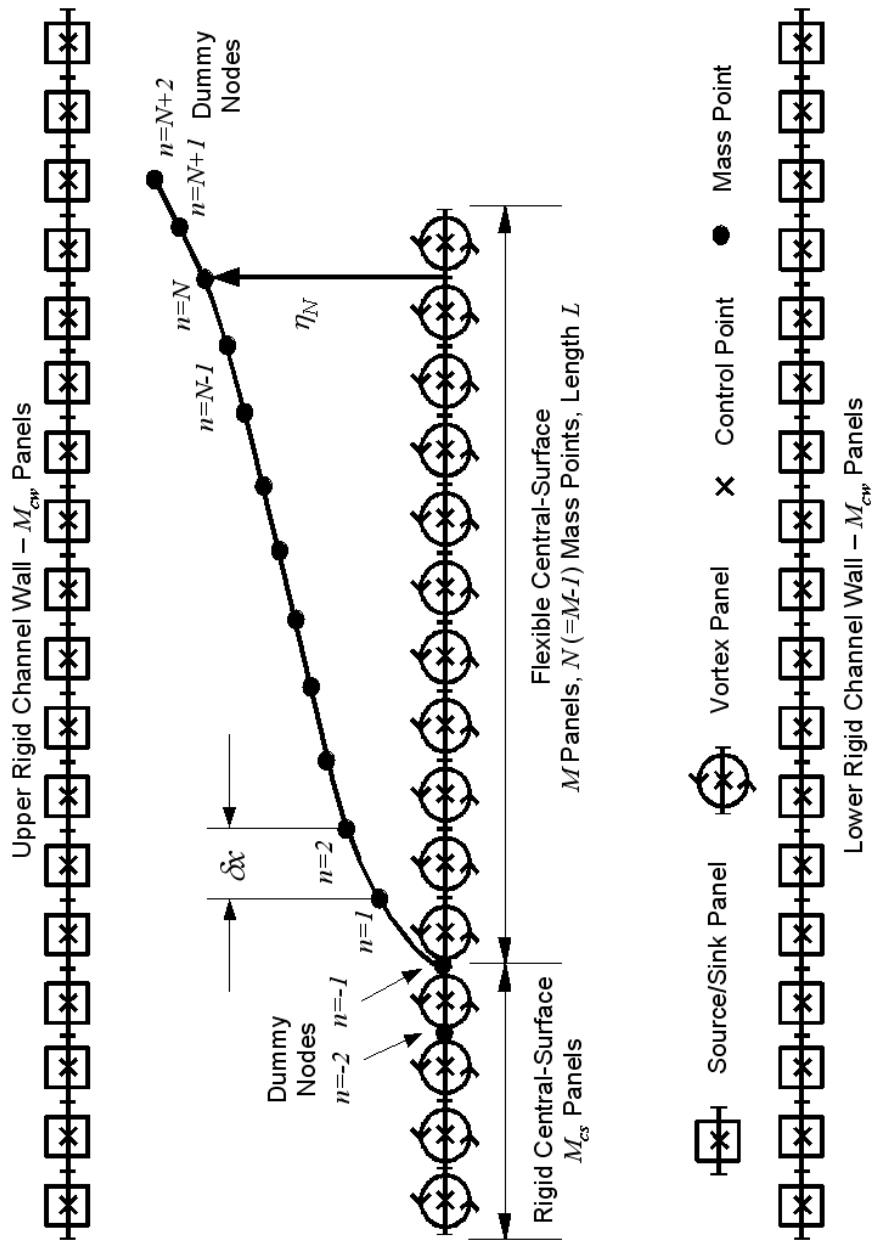
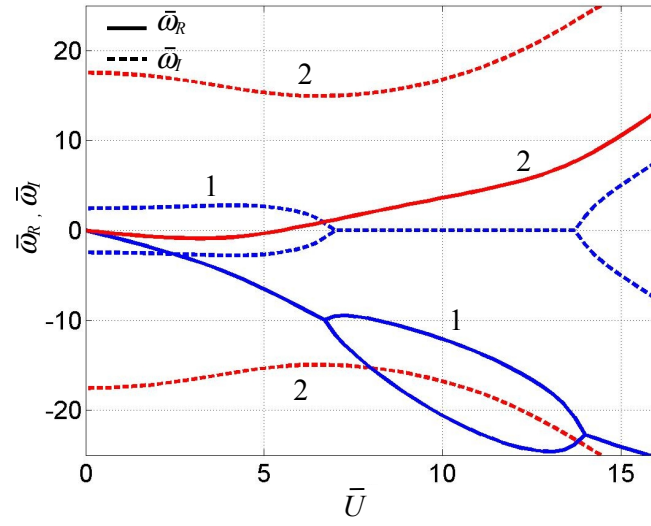
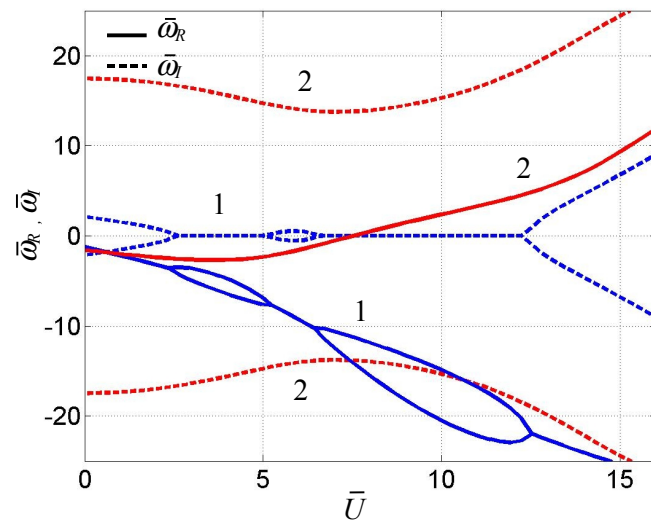


Fig. 2.

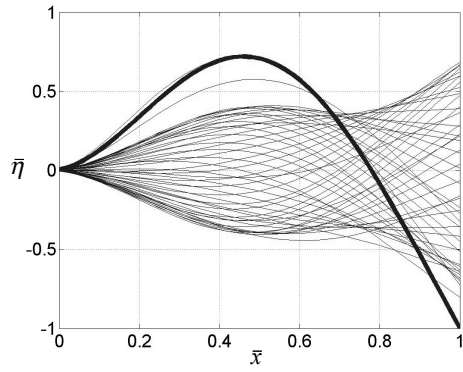


(a)

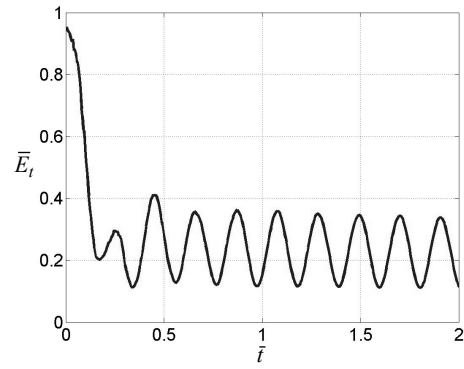


(b)

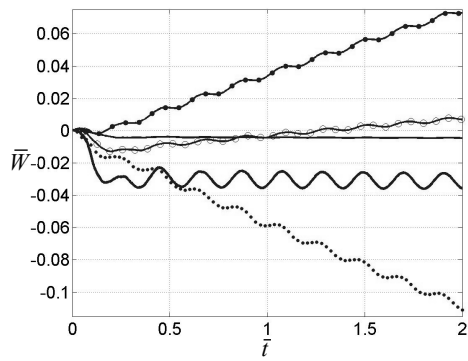
Fig. 3.



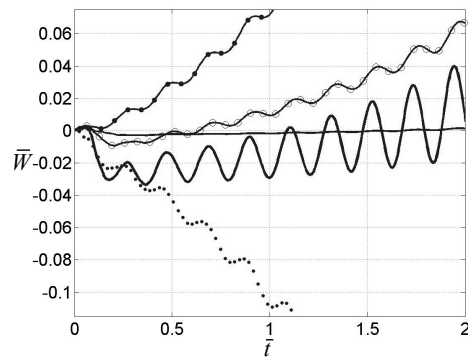
(a)



(b)



(c)



(d)

Fig. 4.

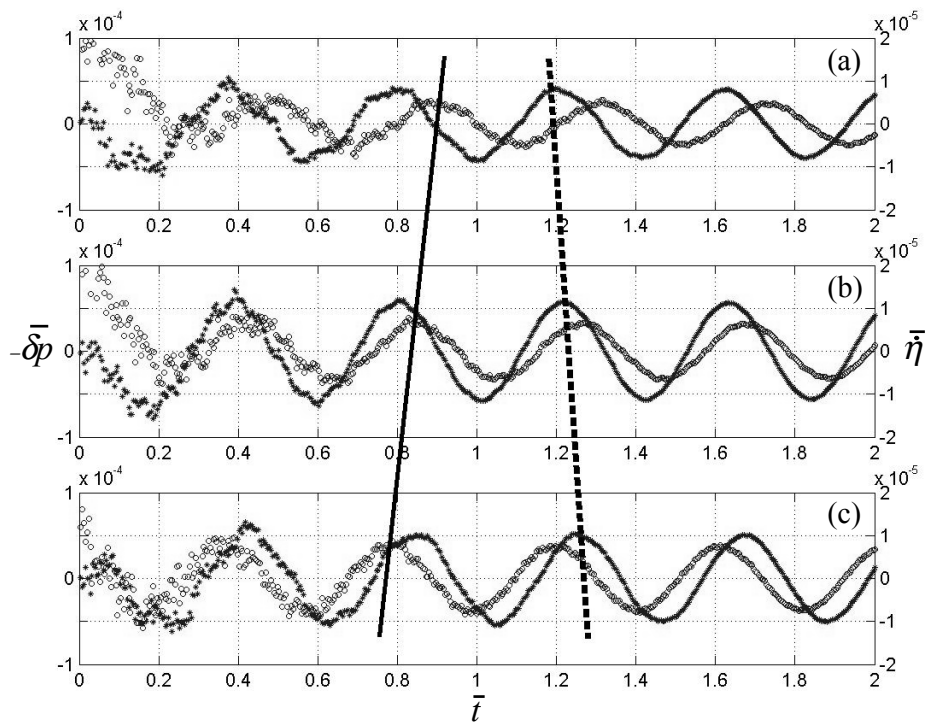


Fig. 5.

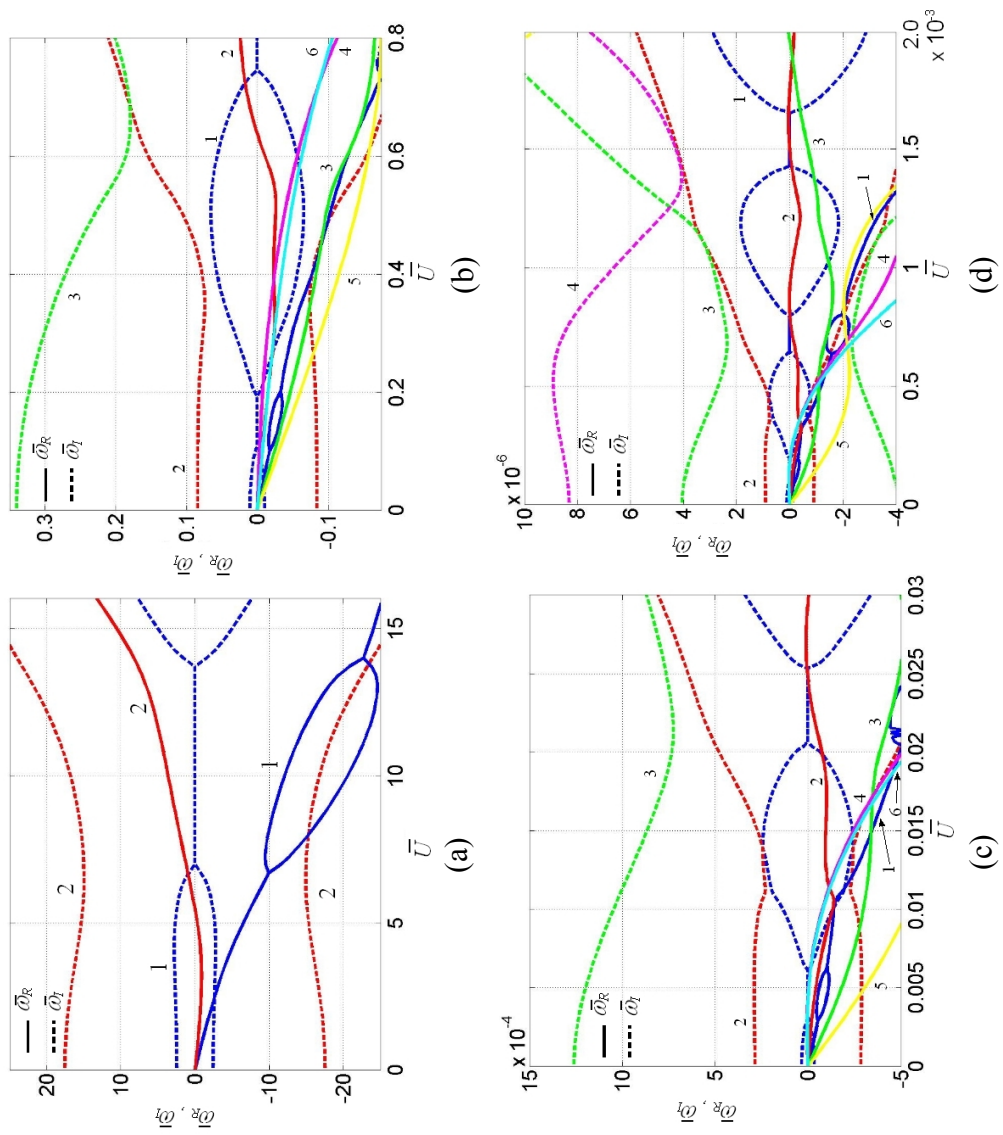
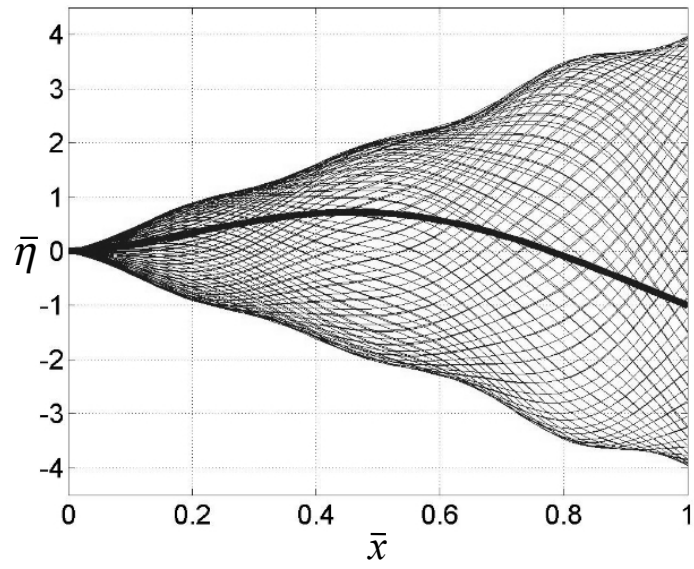
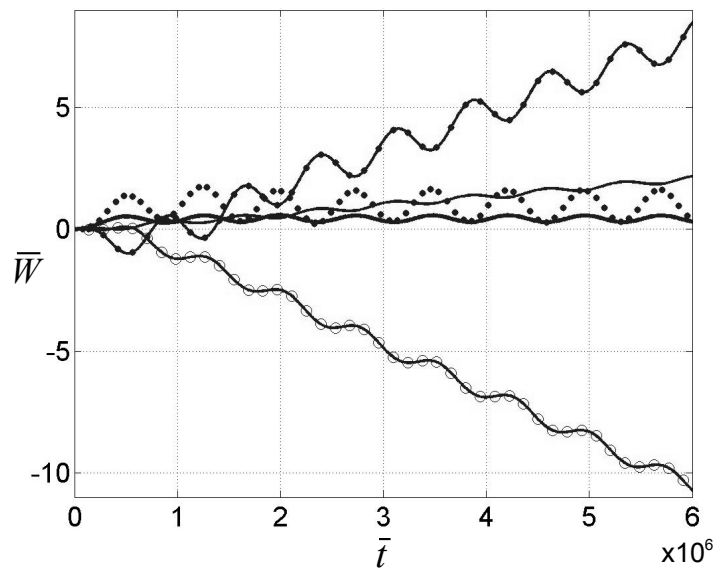


Fig. 6.



(a)



(b)

Fig. 7.

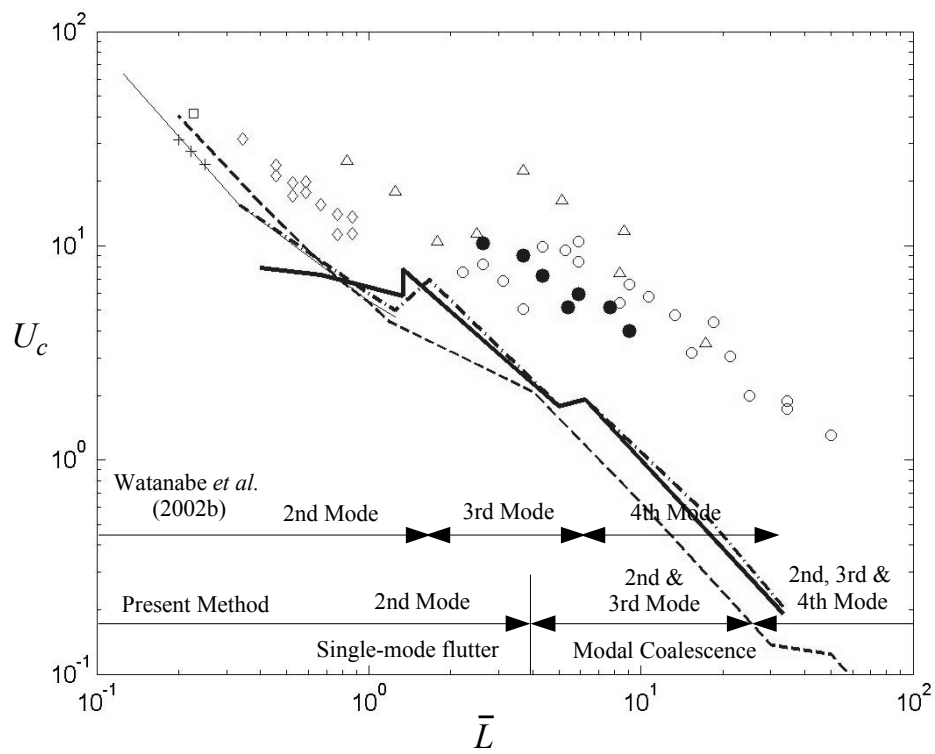
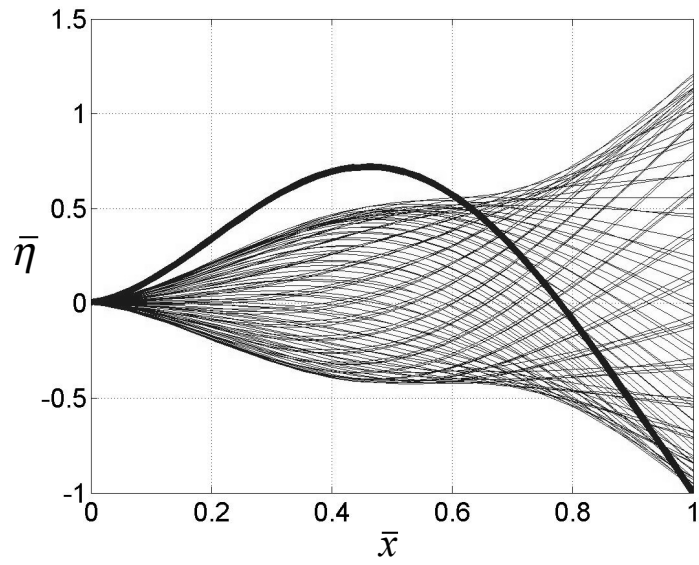
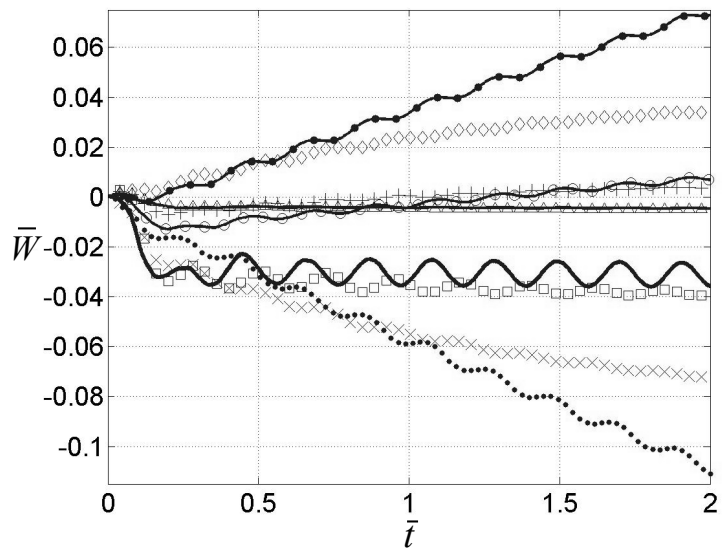


Fig. 8.



(a)



(b)

Fig. 9.

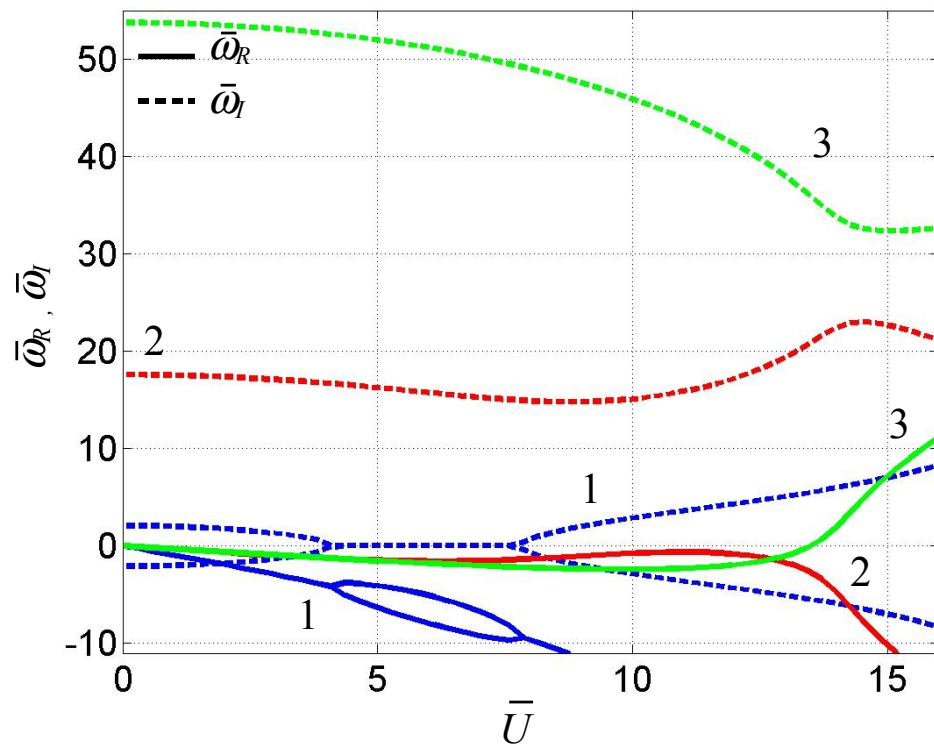
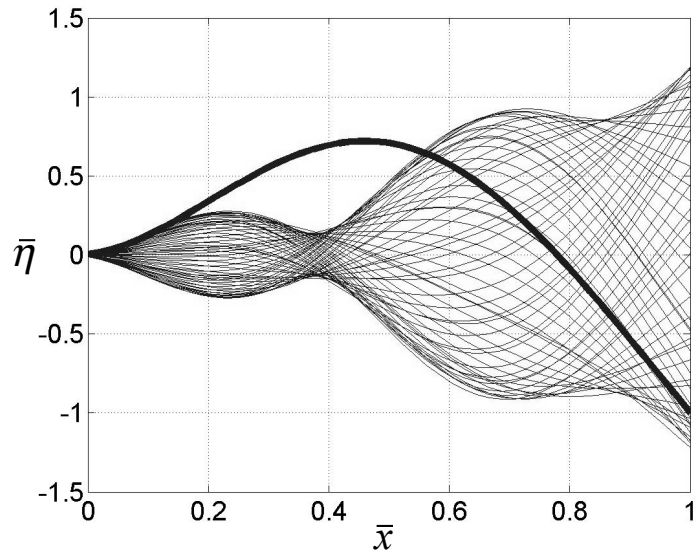
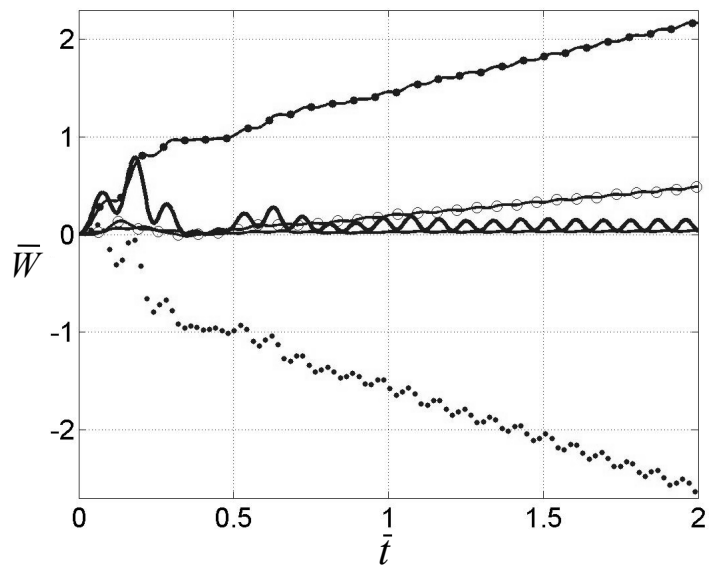


Fig. 10.

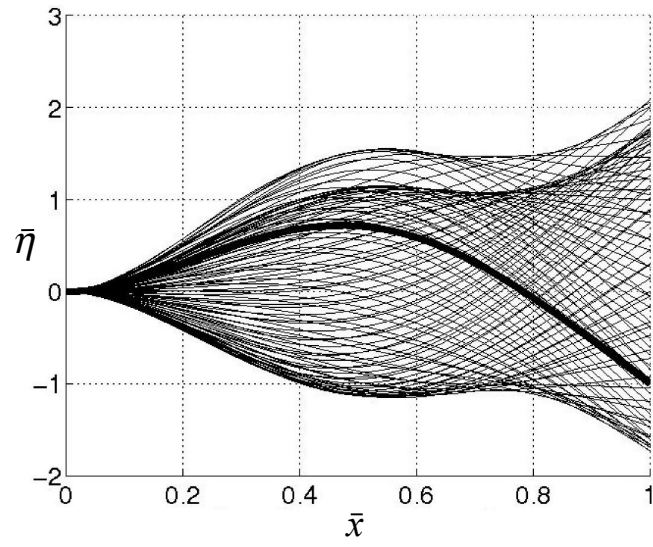


(a)

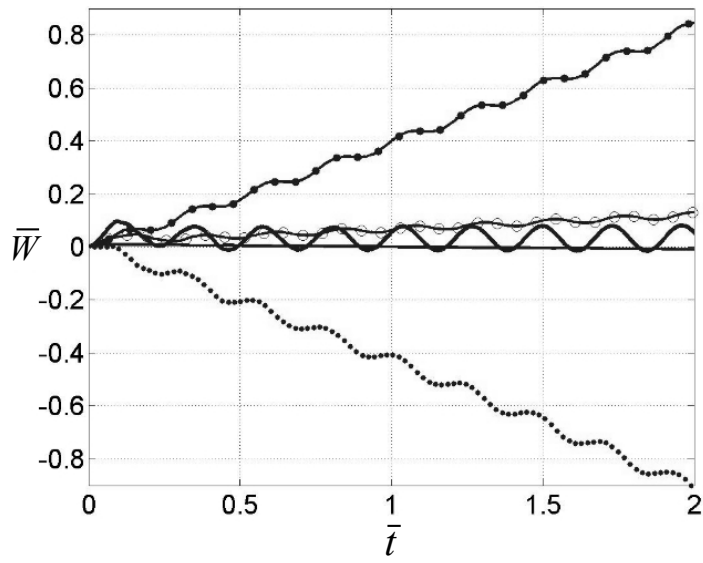


(b)

Fig. 11.

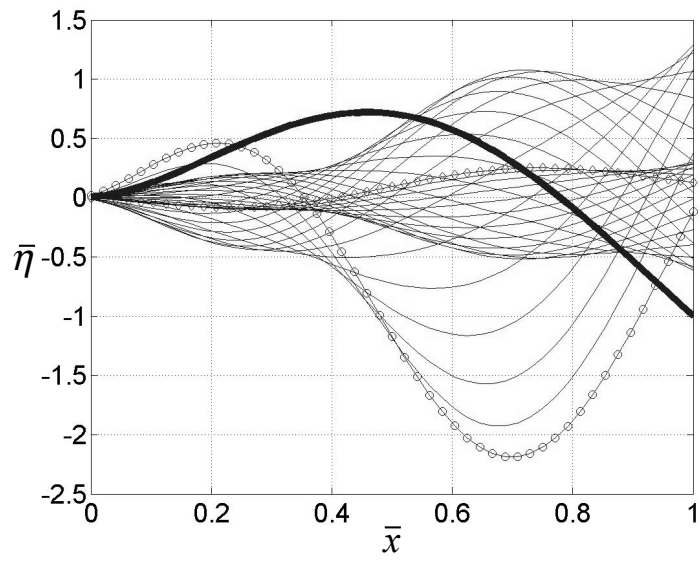


(a)

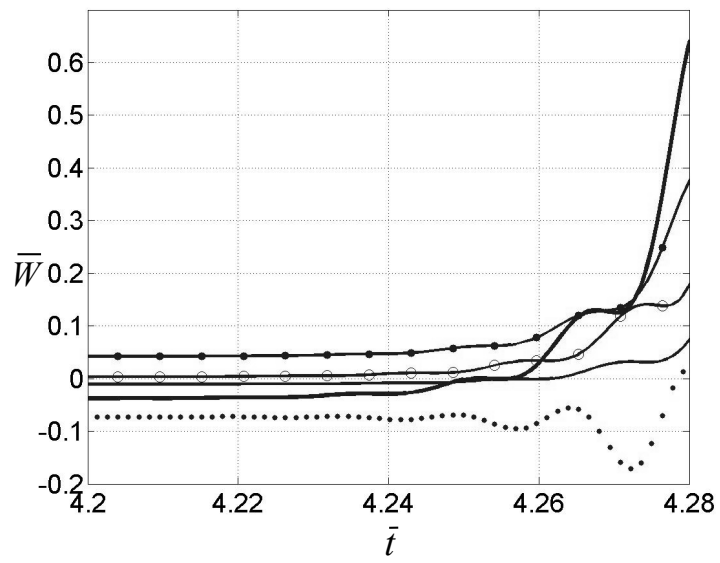


(b)

Fig. 12.



(a)



(b)

Fig. 13.

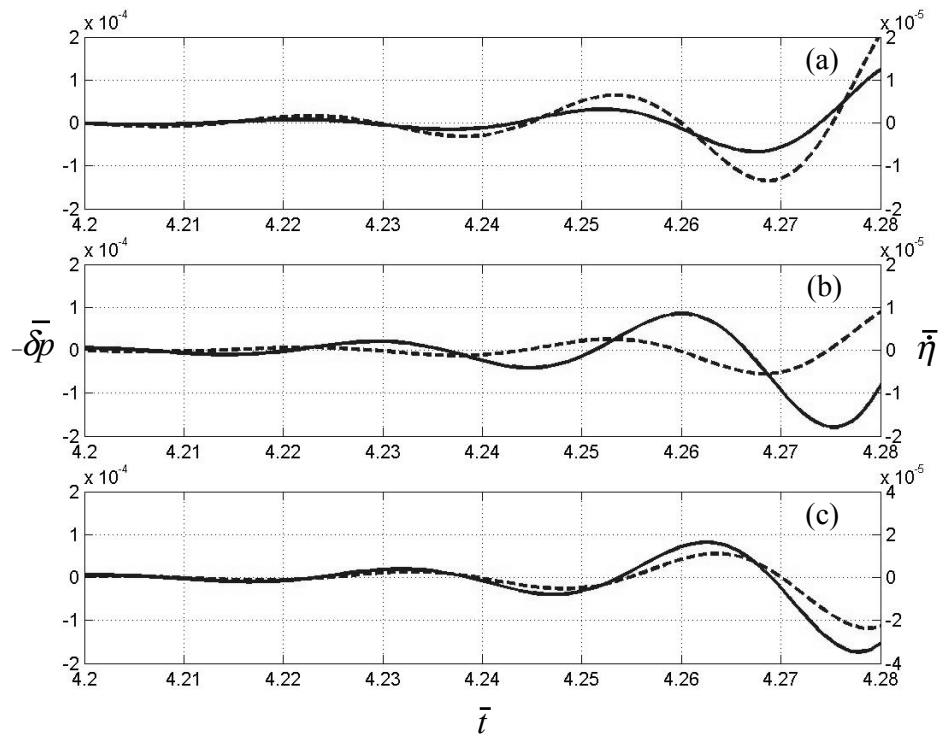
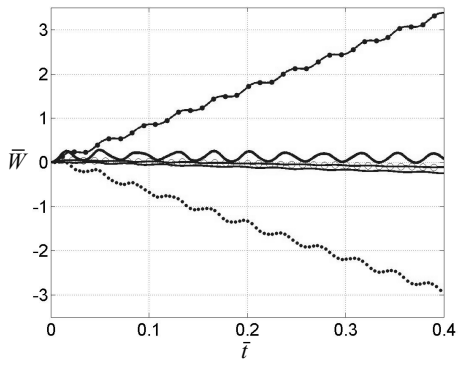
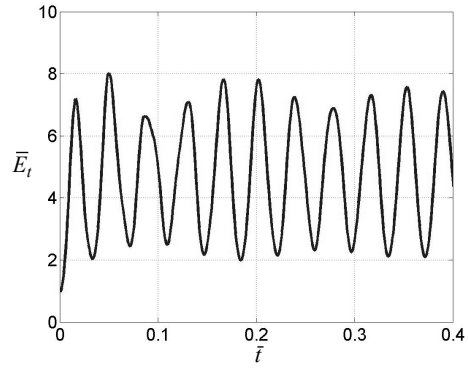


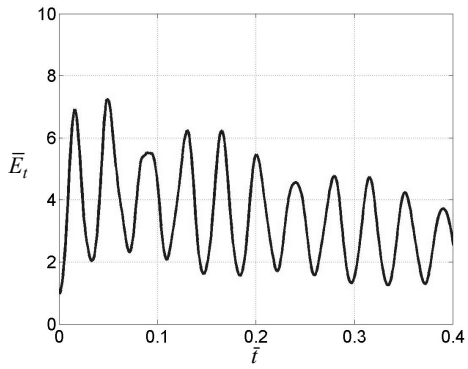
Fig. 14.



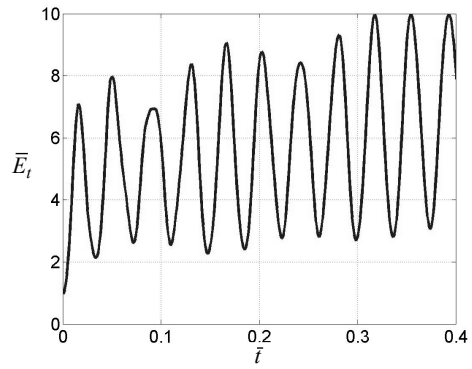
(a)



(b)



(c)



(d)

Fig. 15.